The Dissertation Committee for Loucas K. Loumakos certifies that this is the approved version of the following dissertation:

Fingerprinting of Si surface bonds using non-resonant optical second-harmonic generation

Committee:

Michael W Downer, Supervisor

Alexander A. Demkov

Greg O. Sitz

John G. Ekerdt

Manfred Fink

Fingerprinting of Si surface bonds using non-resonant optical second-harmonic generation

by

Loucas K. Loumakos

Dissertation

Presented to the Faculty of the Graduate School of
The University of Texas at Austin
in Partial Fulfillment
of the Requirements
for the degree of

Doctor of Philosophy

The University of Texas at Austin
August, 2018

Dedicated to my wife and my family.

Acknowledgments

First and foremost I must thank my supervisor, Prof. Michael W. Downer. I believe he one of the "giants" Albert Einstein was referring to, both as a scientist, a teacher and a mentor. This work is only made possible with his scientific guidance, his patience and is financial and emotional support. I am truly blessed to have been a part of his research group.

I would also like to thank my committee members for all their support: Prof. Manfred Fink, Prof. Alexander A. Demkov, Prof. Greg O. Sitz and Prof. John G Ekerdt. Also the graduate advisor Prof. John W Keto. I was fortunate enough to also be their student or their teaching assistant. Special thanks to Dr. Robert Ehlert who not only put together most of the experiment but also taught me almost everything about working in a lab with a laser and a UHV environment. Over the years I have also worked with a lot of my fellow Downer group colleagues. Two of them definitely stand out: Dr. Watson Henderson and Dr. Rafal Zgadzaj. Nonetheless I would like to thank Dr. Yen-Yu Chang, Dr. Junwei Wei, Dr. Xiaohui Gao, Dr. Xiaming Wang, Brandon Furey, Yujin Cho, Adam Ramm, Dr. Hai-En Tsai, Dr. James C. Sanders, Dr. Zhengyan Li, Andrienne Prem and Jesse Stamper. I would also like to thank my friends and fellow RLM inhabitants Dr. Mingsy Chua, Dr. Antonia Cheimonidou, George Stratis and Dr. Yiannis Keramidas for all their help and support.

I am also obliged to a lot of people employed by the University of Texas at Austin as technical and administrative staff: James Halligan, our financial guru, graduate coordinator Matt Erwin, 2nd floor experts Jack Clifford, Ed Baez, Larry Sandofur, Garry Thomas and Rober Hasdorff. Nothing would have been possible without the full support of my wife, my family and the friends that became family, like Antonis Kartapanis, during this long and difficult process.

There are a lot more people which I am grateful for but I will not name them here for lack of space. To those I would like to say: "Thank you, know that you are always in my heart.

Fingerprinting of Si surface bonds using non-resonant optical second-harmonic generation

Publication No. _____

by

Loucas K. Loumakos, Ph.D.
The University of Texas at Austin, 2018

Supervisor: Michael W Downer

Modern electronic device structures require monitoring and control of surface structure at the atomic level during epitaxial growth. We demonstrate an optical fingerprinting technique that isolates, identifies and monitors individual types of bonds (e.g. step-edge rebonds, terrace dimers) and their chemical activity on a single-domain, vicinal Si(001) surface in ultra-high vacuum. The method uses optical second-harmonic generation (SHG) at a single wavelength, but at multiple incidence angles and polarizations (MAP) hence we call it SHG-MAP. SHG-MAP identifies bonds via the unique dependence of their SHG response on azimuthal sample rotation. Using a simplified bond hyper-polarizability model (SBHM), we developed an automated two-step algorithm for identifying all opportunities for isolating a certain bond type geometrically without multi-parameter fitting: firstly, the full parameter space is used to create a 4-D model of the expected macroscopic SHG radiation and secondly a search is preformed to isolate unique bond group contributions. We demonstrate SHG-MAP by monitoring adsorption of atomic hydrogen and chemical etching of rebonded r-D_B steps on clean vicinal Si(001) in ultra high vacuum.

Contents

List of Figures

List of Tables

Chapter One: Introduction

In the years to come we will be looking at the current period as the beginning of the Age of Artificial Intelligence. The Age of Information has long given its place to the Age of Mobility and Connectivity, but, despite the change, the hunger for more computing power has remained unquenchable. Today's processors and microelectronic devices are still wonders of miniaturization. They also must satisfy the demand for low power operation and small heat footprint, especially for the mobile devices, while machine learning demands parallel processing and intrinsic support for complex mathematical calculations. The semiconductor industry, a longtime pioneer in accurate and fast microelectronic manufacturing, will need to adapt once more with more controlled and faster deposition methods on silicon surfaces.

1.1 Overview

In this work we present a non-resonant in-situ optical probe capable of identifying and isolating — i.e. "fingerprinting" — individual types of Si-Si bonds and their chemical activity using surface optical of Second Harmonic Generation (SHG) driven by a compact, fixed wavelength ultrafast laser.

Spectroscopic methods such as infrared absorption, Raman scattering, and infrared-visible sum-frequency generation (SFG) are the most well-known surface

bond fingerprinting techniques. However, infrared absorption and Raman scattering are very weak at surfaces (without special enhancement techniques) [7] and lack inherent surface specificity, while SFG is equipment-intensive. All of these spectroscopic methods become challenging for surfaces at which differently-oriented bonds of identical chemical composition, and thus similar vibrational frequencies, must be distinguished, or at which vibrational frequencies are very small. The non-spectroscopic SHG method discussed here is inherently surface-specific, and identifies a bond type with a specific surface orientation via the unique dependence of its SHG response on azimuthal sample rotation and polarization. Instead of varying or measuring frequency, the method uses multiple incidence angles and polarizations (MAP). Hence we call it SHG-MAP.

Though the study of SHG began by concentrating on the phenomenon itself and has been studied widely both theoretically [8–12] and experimentally [13–18] once the symmetry dependency of it was realized, it has been gaining ground as an interface sensitive method [19]. Small femtosecond laser oscillators exploit the dependence on the square of the incident intensity to generate strong signals while minimizing surface heating. The resulting convenience has propelled SHG to the forefront of surface science [20].

Our SHG fingerprinting method, SHG-MAP, relies on a single domain surface or interface of a centrosymmetric bulk material with initially well-defined and well-known surface bond orientation. Clean reconstructed vicinal Si(001) surfaces

can satisfy these criteria. It possesses an almost single domain surface with double atomic steps interrupting the terraces. Such steps are not only crucial in determining the chemical and electronic properties of the surface [21, 22] but also as preferred adsorption sites for heteroepitaxial growth of group III-V semiconductors [23, 24].

The ability to vary the size of the step by controlling the offcut angle and the annealing temperature [25] has made vicinal surfaces useful as templates for self-assembled growth of nanostructures [26, 27]. The centrosymmetry (and thus lack of SHG susceptibility) of the underlying bulk silicon, together with the low symmetry, and strong SHG anisotropy of clean reconstructed vicinal silicon make it well suited for SHG-MAP studies[28].

The analysis of such results in the absence of first-principle calculations [29] is usually performed macroscopically with azimuthal Fourier analysis or microscopically with the Simplified Bond Hyperpolarizability Model by Aspnes et al. [30]. However, both methods have drawbacks, discussed in Chapter 2, that hinder the accurate explanation [31, 32] of adsorbent processes on the surface, even when initial atomic positions are well known [33]. Thus, we have developed [1] and expanded SHG-MAP a non-resonant optical geometrical bond isolation method based on SBHM. Our method avoids the complicated multiparameter fitting by predicting the SHG response of individual bond groups through the full parameter (incidence angle, incoming polarization, azimuthal angle, observing polarization) and algorithmically selecting an isolation geometry for each bond in a "picked out of the crowd" strategy.

We demonstrate this method by observing hydrogen etching of rebonds on vicinal Si(001). However, the method is applicable to many other centrosymmetric materials.

1.2 Scope

In Chapter 2 we present our experimental setup: the ultra high vacuum environment, the sample surface manipulation tools and our surface sensitive diagnostic tools. In the second part we present previously used methods of analyzing experimental SHG results: azimuthal Fourier decomposition and the SBHM. The third part presents experimental results, of clean and hydrogenated Si(001) along with a brief analysis.

In Chapter 3 the SHG-MAP framework is introduced in the first part with its predictions for clean vicinal Si(001) in the second. Finally in the third part, we demonstrate SHG-MAP by monitoring adsorption of atomic hydrogen and chemical etching of rebonded r-D_B steps on clean Si(001).

Chapter 4 presents some ideas for future experiments and improvements on SHG-MAP followed by the Appendices A,B and C containing more details on our equipment and algorithms.

Chapter Two: Surface Sensitive Diagnostics: Experimental Methods and Analysis

Driven by a constantly increasing demand for faster, cheaper and more mobile, modern electronic devices continue to stretch the limits of nanostructure manufacturing. However, with each advancement, more possibilities for errors are introduced leading to the need for fast, simple and non-invasive methods for monitoring the self-organized growth of nanostructures [34]. In this chapter we set the framework which, in the second chapter, will lead to a new faster, and more accurate method of non-resonant optical in-situ monitoring. We start by presenting the diagnostic tools available in our experimental setup and current methods of analyzing the experimental results both macroscopically and microscopically. We then present our surface of choice, clean reconstructed vicinal Si(001), as well as previous relevant studies from our lab.

2.1 Diagnostic Tools and Experimental Setup

2.1.1 Ultra-high Vacuum Chamber

It is crucial to perform our experiment in an ultrahigh vacuum (UHV) chamber to avoid contamination or unintended adsorption on the surface structures of interest. Our UHV chamber, seen in Fig. 2.1, was designed and built by Dr. Robert Ehlert as

part of his PhD project. A list of all the major components is presented in Appendix A, Tab. A.1 along with more information about maintaining a vacuum of 10^{-11} Torr range. The chamber is cylindrical with about 30 cm in radius and approximately 120 cm in height. It allows for a sample to be positioned in approximately the middle with external manual controls for the XYZ direction, while mechanized computer controlled azimuthal rotation is available. The sample can be replaced without breaking vacuum using a "wobbling stick" located in a long transfer arm. The triangle arm is connected to the chamber through a valve gate capable of holding vacuum while being exposed to atmospheric pressure. Thus, under normal operation, the chamber always remains in UHV, avoiding the time and labor consuming process of "baking". There are many viewing ports with some having optical windows appropriate for a laser beam to be incident on the sample. There is also a strain-free optical port suitable for RAS. The laser port provides incident angles of 7.5°, 22°, 30°, 45°, and 52° while the strain-free optical port is located at normal incidence. The chamber is also equipped with a low energy electron diffraction system (LEED), presented in subsection 2.1.4, and a Quadrupole Mass Spectrometer (QMS) capable of 0.5 atomic mass units (amu) in the 1-200 amu range. We have the ability to introduce gases and liquids in the chamber. More details are given in Appendix A. There are two different ways of heating the sample. A filament located behind the sample can heat it resistively up to 1000° K. A filament capable of cracking hydrogen is also present. Secondly, a current can be passed directly through the sample radiatively heating it

up to 1500° K.

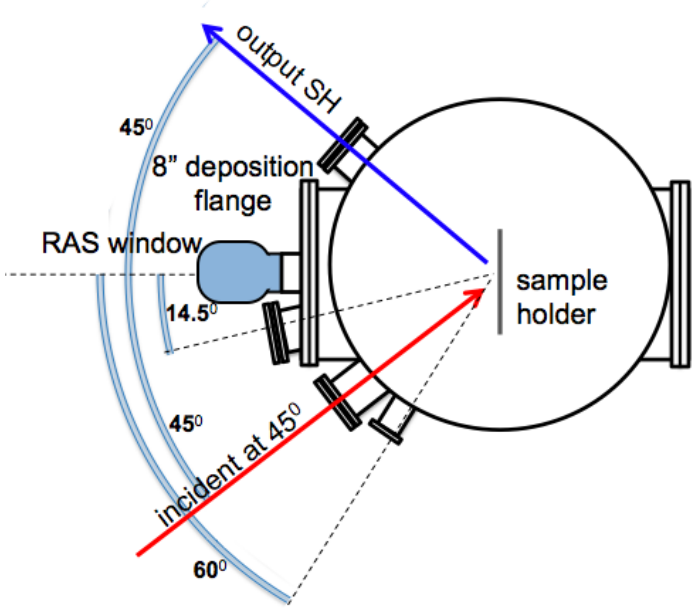

Figure 2.1: A schematic of the chamber showing the available optical ports.

2.1.2 Second Harmonic Generation

Optical second harmonic generation (SHG) was finally observed by Franken et al. [8] in 1961. He used a ruby laser beam to traverse a quartz crystal so the resulting SHG signal was very low. SHG suffered not only experimentally, but also theoretically until Bloembergen incorporated the nonlinear properties of matter into Maxwell's equation [10]. A common qualitative description of SHG involves the Lorenz oscillator model of an atom with Coulomb force as the attractive force. The bond electron oscillates in an asymmetric, anharmonic local potential in noncentrosymmetric media which produces significant deviation from a perfect parabola at

large amplitudes as seen in Fig. 2.2. Thus, the produced electric field differs from the original monochromatic, and its Fourier decomposition contains higher orders as well as the fundamental and DC as shown in Fig. 2.3.

$$P_i^{(2\omega)} = \epsilon_0 \chi_{ijk}^{(2)} E_j^{(\omega)} E_k^{(\omega)} + \epsilon_0 \chi_{ijkl}^{(Q)} E_j^{(\omega)} \nabla_k E_l^{(\omega)} \tag{2.1}$$

In centrosymmetric media, even-order harmonics vanish, leaving odd-order harmonics. However, on the surface of centrosymmetric media, like silicon, the symmetry is broken. Thus producing an SHG signal, which in the dipole approximation originates mainly at the surface with a very small quadrupole or magnetic dipole term, as shown in Eq. 2.1, where $\chi_{ijk}^{(2)}$ is the second harmonic effective interface susceptibility caused by inversion symmetry breaking and electric field discontinuity on the interface.

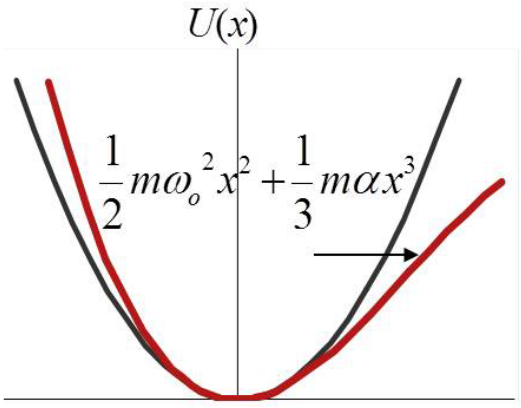

Figure 2.2: A harmonic vs anharmonic potential.

2.1.3 Rotational Anisotropy Spectroscopy

Reflectance anisotropy spectroscopy (RAS) was first suggested in 1977 as an ellipsometric setup operating at normal incidence. At normal incidence the plane of

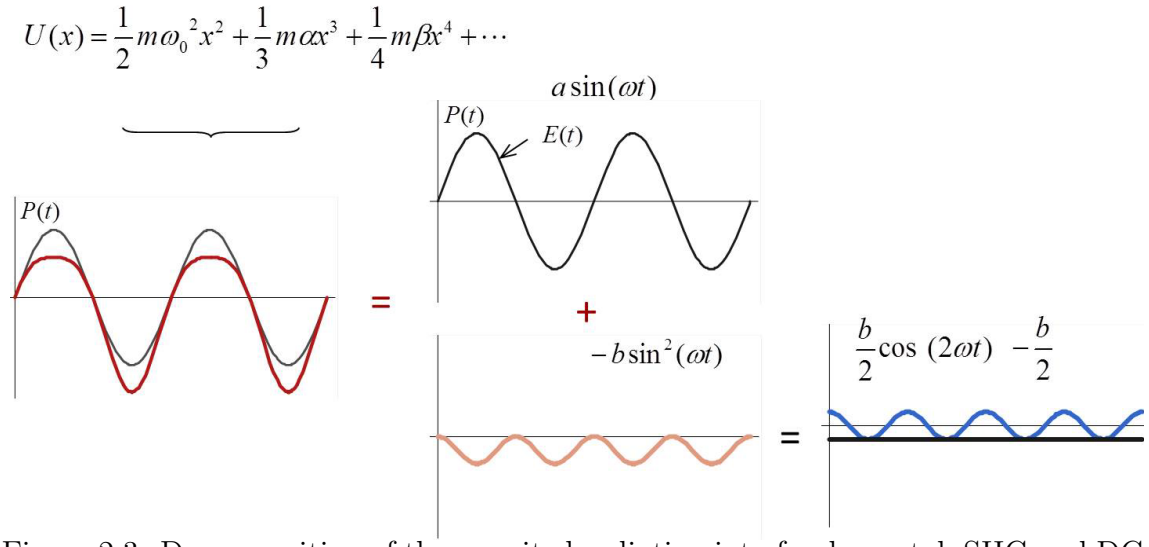

Figure 2.3: Decomposition of the emmited radiation into fundamental, SHG and DC.

incidence is not defined anymore, and on an isotropic cubic crystal the amplitude ratio and phase difference approaches a trivial value of 1 or 0. Therefore, the RAS signal originates in the reduced symmetry areas of surfaces and interfaces. This makes RAS a perfect probe for stepped surfaces, as it distinguishes anisotropic step edges and single-domain terraces from the isotropic bulk [35]. It is also sensitive to adsorbates and can be modeled by first-principle calculation. Due to the fact that it has great sensitivity, early experiments which used a rotating sample suffered from "wobbling during rotations. Aspnes et al. [36] developed a technique that uses a photoelastic modulator (PEM) to avoid rotation and allow both the real and imaginary part of the signal to be measured simultaneously. The incidence light is polarized in a 45° angle of the main sample axis and the reflected light is modulated by a PEM before going through an analyzer, as seen in Fig 2.4. The complex reflectivity ratio, which

in silicon is about 10^3 weaker than reflectance, is

$$\frac{\Delta r}{r} = 2\frac{r_{[\bar{1}10]} - r_{[110]}}{r_{[\bar{1}10]} + r_{[110]}} \tag{2.2}$$

for (001) faces. More information about out RAS setup is given in Appendix B.

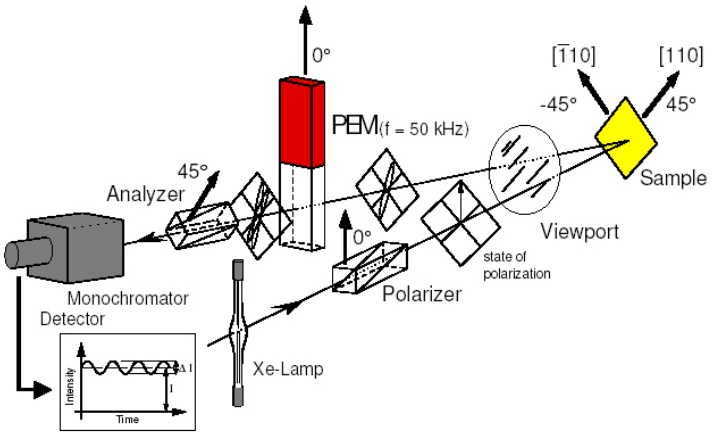

Figure 2.4: A schematic of our RAS setup

2.1.4 LEED

Low energy electron diffraction (LEED) is an established method of in situ surface characterization. It utilizes the fact that low energy electrons, 20-300 eV, can only interact elastically with the first 4-5 atomic layers of a sample. Although this was long known, the practical difficulties associated with LEED apparatus and its extreme surface sensitivity kept it from use until the 1970's. After these problems were dealt with, LEED became a common tool of in situ surface characterization mainly due to its ease of use and high resolution. LEED can provide detailed structured

determination of many nanomaterials, either periodically ordered [37] or isolated nanostructures [38], because of its high resolution.

The first electron diffraction experiment was performed by Davinson and Germer in 1927 [39], thirty years after the electron beam was discovered by J.J. Thompson. Their apparatus, which is quite similar to modern Low Energy Diffraction (LEED) systems, was constructed to demonstrate the wave nature of electrons. However, LEED was abandoned for a number of years due to several reasons. Firstly, it was easier to produce and control electron beams with higher energy, which could also penetrate deeper into the sample. Secondly, it was difficult to acquire a low energy electron signal since only a small fraction, around a twentieth of the incident electron beam, would produce a diffraction pattern. Thirdly the diffracted beam was highly affected by the specific surface region. This meant that oxides or other adsorbents on the surface would affect the diffraction pattern, and, at the time the methods to clean the surface and maintain it were not available. Lastly, the analysis of LEED results suffered from insufficient or cumbersome theories and many researchers were discouraged [40]. The atomic scattering factors where not known precisely, the absorption corrections were only qualitatevely understood, the internal potential corrections could not be made accurately and the beam energy width was quite large at the time. [41]. One of the researchers that stayed in the field from the beginning was H.E. Farnsworth at Brown University [42]. He is responsible for much of the early developments in LEED.

By the 1970's techniques to clean the surface, such as ion bombardment and flashing to high temperatures, became available as well as ultra high vacuum (UHV) systems which kept the surface clean from oxidization or other adsorbents for hours instead of minutes. The sensitivity to the immediate surface region, which was previously a problem, became one of the best advantages of LEED compared to other study methods.

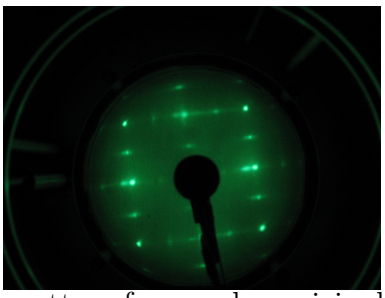

Figure 2.5: LEED diffraction pattern from a clean vicinal Si surface in a UHV system.

Improvements to the apparatus like [43–45] the "double grid repeller system to improve electron resolution" [46], a pulsed beam for rapid precision measurements, [47] and the introduction of the post acceleration grid in 1964, [48] allowed researchers to take advantage of the possibilities of LEED as a surface characterisation method. Fig. 2.5 shows an example of a LEED diffraction pattern from a clean vicinal Si surface in a UHV system. With a relatively simple setup and a resolution of 2.7$\mathring{A}$ at 20 eV LEED is one of the preferred methods for in situ surface probing. More information about the LEED used in our experiment is presented in Appendix A.

2.2 Analysis of SHG Results

The two most common methods of analyzing SHG data is to attempt a phenomenological description using Fourier coefficients or a simplified microscopic model like SBHM [49]. Here we present in brief both these methods.

2.2.1 Fourier Decomposition

If Fourier decomposition we assume that the harmonic field generated at the surface can be expressed phenomenologically as the following Fourier sum, for a polarization combination:

$$E_{p,p}^{(2\omega)} = \sum_{j=0}^{4} a_j^{p,p}(\omega) cos(n\phi) \tag{2.3}$$

where $a_j^{p,p}$ are linear combinations of products of Fresnel factors and tensor components of the second order nonlinear susceptibility [6]. In general the coefficients $a_j^{p,p}$ and for a third-rank surface dipole susceptibility tensor can only be five of them, including $a_0^{p,p}$.

2.2.2 SBHM

Until now a macroscopic continuum model utilizing surface symmetry has provided the most commonly used description of second harmonic generation. Simplified bond hyperpolarizibility models have emerged as an intermediate approach between phenomenological Fourier analysis and complicated microscopic models. They allow

SHG data to be interpreted directly in terms of the microscopic properties of a few individual bonds and can be calculated ab-initio. The SHG signal can then be interpreted as the far-field intensity of the square of the superposition of fields radiated by the anharmonic component of the bond charge motion.

SBHM was developed by Aspnes et al. [49] and it basically expresses the macroscopic second harmonic field as

$$\vec{E}_{p,p}^{(2\omega)} = \frac{k^2 e^{ikr}}{r}(\hat{I} - \hat{k}\hat{k}) \sum_j (\beta_{2j}^{\parallel} \hat{b}_j \hat{b}_j \hat{b}_j) \cdot \vec{E}\vec{E} \tag{2.4}$$

where the sum is the SH dipole moment, $\beta_{2j}^{\parallel}$ the axial hyperpolarizibilty, and $\hat{\beta}_j$ the direction of the j-th bond, and the sum runs over bonds in a surface unit cell. $\vec{E}$ is the fundamental field, $\hat{I}$ the unit tensor and k the vacuum wave number of the SH field. $\beta_{2j}^{\parallel}$ are assigned to selected bonds in the surface unit cell, and their (in general complex) values determined by empirically fitting their collective far-field SH radiation pattern to rotationally anisotropic SHG date at each wavelength.

SBHM makes a number of simplifications and assumptions: firstly the components of the hyperpolarazibility and polarizability tensors arise from charge motion to the bond axes are neglected. Secondly the local field factors are implicitly folded into $\beta_{2j}^{||}$.

For the case of our vicinal Si(001) the bond parameters (bond length,polar angle, azimuthal angle) were calculated by Pehlke et al [50] for 0°K. Ab-inition calculations were also performed by Prof. A. Demkov and Dr. O. Sharia. More information about the calculation can be found in [1].

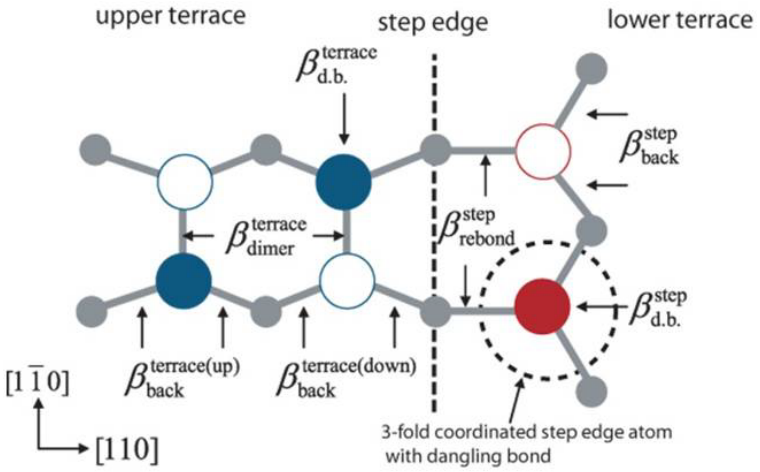

Figure 2.6: Top-down schematic of the clean vicinal Si(001) with an $2° - 8°$ offcut towards [001]. We use the bonds shown here of, the terrace and step-edge structure, in assigining bond hyperpolarizability for use in SBHM analysis. The smallest filled grey circles represent second-layer Si atoms. Larger circles represent up-(large filled) and down-(smaller open) buckled Si dimer atoms. Charge-rich dangling bonds extend approximately vertically upward from the up-buckled Si dimer atoms, and thus are also represented by large filled circles [1].

In order to perform a meaningful SBHM analysis we need to reduce the number of free parameters. Even the reduced unit cell of Fig. 2.6 contains 22 bonds with complex hyperpolarizabilities thus 44 parameters. In practice [30, 51] we need at most 7 for a meaningful analysis.

2.3 SHG of Vicinal Si(001)

This section presents SHG measurements on a vicinal, reconstructed Si(001) performed by Dr. Robert Ehlert and the author in subsection 2.3.3. A more detailed analysis of these results is presented in Ehlert's PhD thesis [1]. The results are presented here in brief to establish continuity and also to demonstrate some of the

disadvantages of traditional multi-parameter fitting.

2.3.1 The Vicinal Si(001) Surface

Vicinal Si(001) surfaces, silicon miscut a few degrees from [001], are attractive templates for growth of nanoscale structures [49] and single crystal organic monolayers [52]. Their double atomic length (D_B) step edges exhibit high chemical affinity for many adsorbets providing templates for growth of nanowires [53]. Also, their strong dimer-like Si=Si "rebonds" are oriented perpendicular to the D_B steps. They tend to stabilize the step-edge structure while forcing terraces into a single-dome $c(4 \times 2)$ reconstruction which orders Si=Si dimer rows [54, 55]. This makes them great templates for growth of crystalline organic layers [56]. In order to get this clean surface we follow a procedure developed by Hata et al [57] where the sample is heated overnight at about 600° K and then flashed to 1050° K for 30 seconds through resistive heating. We check the LEED pattern for a clear (2×1) reconstruction with only weak (1×2) spots and the characteristic splitting of primary spots caused by the periodicity of D_B as seen in Fig. A.8.

Clean semiconductor surfaces, either cleaved or annealed, experience relaxation, reconstruction and step formation to lower their surface energy. Clean Si(001) lowers surface energy mainly by forming dimers using half of its two dangling bonds, forming a (2×1) symmetric dimer model, as shown in Fig. 2.7(a).

Then degenerate dangling bond states of the symmetric dimers further reduce

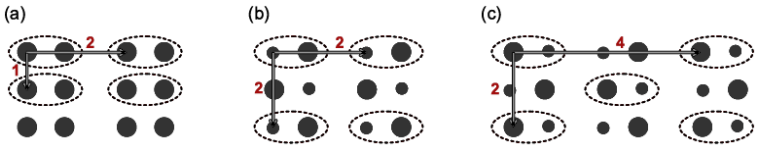

Figure 2.7: Top view of (a) (2×1), (b) (2×2) and (c) c(4×2) reconstructed Si(001) surfaces. In the buckled dimer reconstructions (b) and (c) the larges circles protrude further out of the surface than the smaller circles. The arrows show surface unit cells. Taken from [2].

their electronic surface energy by undergoing a Jahn-Teller type slitting of the degeneracy. This causes the dimers to buckle, alternatively due to elastic coupling, and transfer electron density from the lower to the upper atom, forming the energetically preferred c(4x2), as seen in Fig. 2.7(c). This creates a strong electric field across the surface [58]. At room temperature the dimers rapidly switch their orientation leading to the observed (2×1) Fig.2.8. The energy is further lowered by forming steps. The

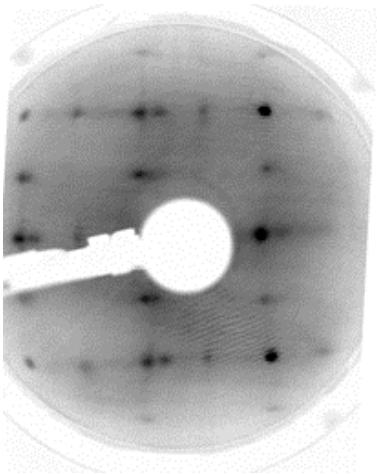

Figure 2.8: The LEED pattern from a vicinal, reconstructed Si(001)surface using 60 eV electrons. A clear (2×1) reconstruction is visible with only weak (1×2) spots. The characteristic splitting of the primary spots is caused by the periodicity of D_B [1].

step height depends on the offcut angle and on the annealing temperature. In angles 2° - 8° double atomic steps [33] are dominant leading to a single domain surface [59]

in contrast with single steps where the terrace dimers alternate between being parallel or perpendicular to the step-edge as show in Fig 2.10 At D_B surfaces of Si(001) with the offcut along the [110] direction, the steps undergo dimer-like rebonding with adjacent surface atoms creating a unique triagonally bond Si atom at the step-edge as shown in Fig 2.9. Just like the terrace dimers, the r-D_B step is buckled.

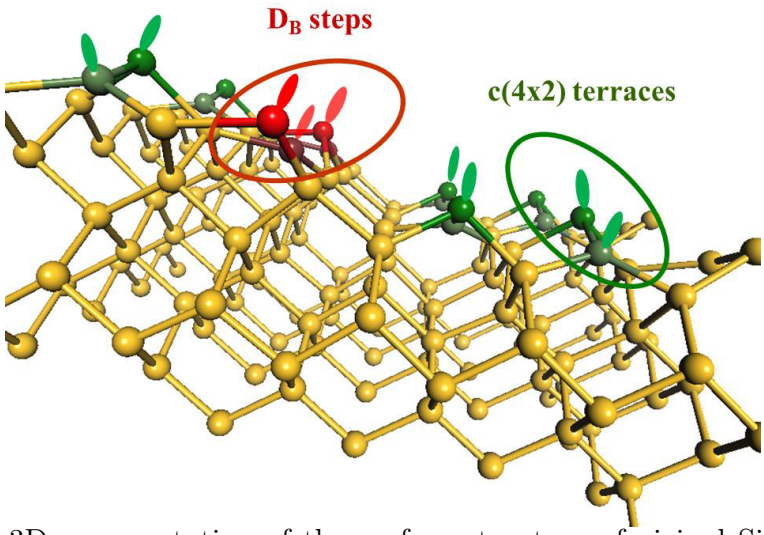

Figure 2.9: A 3D representation of the surface structure of vicinal Si(001) $c(4 \times 2)$ with double atomic height rebonded r-DB steps. Basen on an ab-initio calculation courtesy of O. Sharia and A.A. Demkov. Taken from [1].

There has been great interested in the hydrogen interaction with Si(001) surfaces. Hydrogen at the step sites affects the growth of single crystal silicon films and serves as a model system for adsorbates. The H_2 sticking coefficient for dissociative adsorption increases with sample temperature and adsorbed hydrogen atoms tend to form 1-D chains along the step edges. Atomic hydrogen, acquired near the surface with the help of a hot "cracking" filament, terminates all the dangling bonds, breaks dimers and partially etches the surface by desorbing SiH_{2+} units at room tempera-

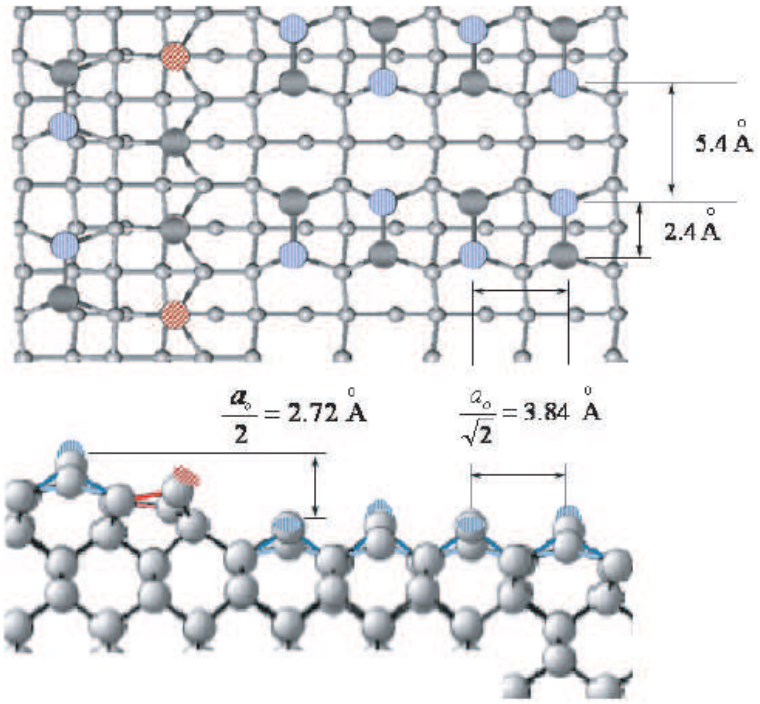

Figure 2.10: Top and side view of reconstructed vicinal Si(001). Blue (Red) dashed balls represent the dangling bonds on the buckled terrace dimers (rebonded DB steps) [2].

ture. At saturation levels this leads to a slightly disordered hydrogenated dihydride surface with large patches of ordered di-hydrogenated Si atoms.

At elevated temperatures though (600°) it is not stable and the terrace dimer structure is maintained, with dangling bonds bound to a single H atom creating a monohydride surface. The rebonded r-D_B steps stability to atomic hydrogen also depends on surface temperature and hydrogen partial pressure even at those high temperatures where dimers are stable as shown in Fig. 2.11.

Molecular hydrogen dissociative adsorption has been harder to study due to its really low sticking coefficients on terrace dimer dangling bonds and the effects of defects and steps on adsorption rates. It selectively saturates step dangling atoms

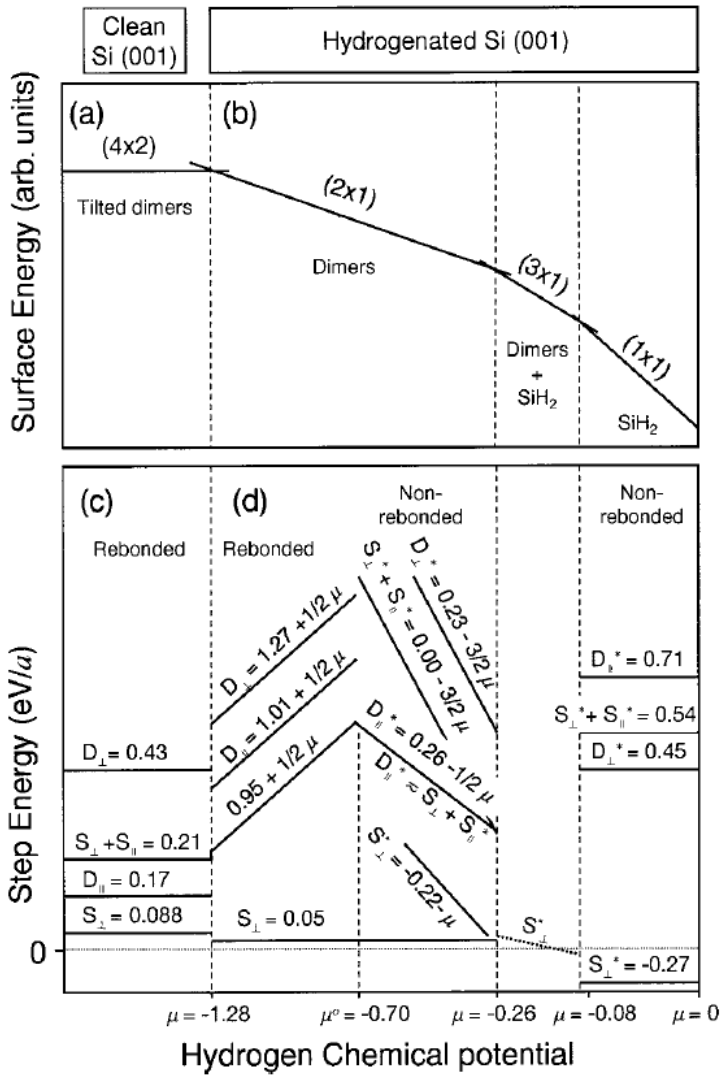

Figure 2.11: Formation energies of surface reconstructions and steps on Si(001): (a) Clean (4×2) phase, (b) hydrogenated (2×1), (3×1), and (1×1) phases, (c) steps on clean Si(001) and (d) steps on the (2×1) and (1×1) phases [3].

with a sticking coefficient of 6 orders of magnitude greater than that of terrace dangling bonds. This was investigated by Hofer et al. [4, 49, 60]: in order for H_2 to rehybridize with the dangling bonds it is necessary for the dimers to be unbuckled thus closing the surface bandgap. This is easier at higher temperatures as seen in Fig. 2.12 indicating that there is significant phonon interaction. However the strong pi interaction of the terrace dangling bonds once the dimers become unbuckled opposes hydrogen adsorption while the step dangling bonds have no such interaction. The high difference of sticking coefficient at room temperature allows us to selectively terminate step edge dangling bonds with a dose of 1800 Langmuir achieves complete step termination [61].

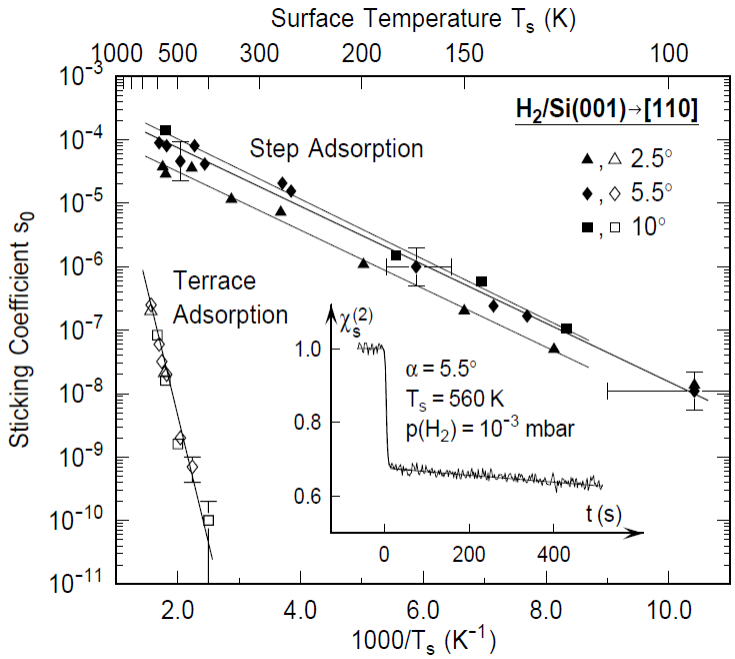

Figure 2.12: The sticking coefficients for room temperature molecular hydrogen on the steps (solid symbols) and terraces (open symbols) of vicinal Si(001) surfaces at various surface temperatures [4].

2.3.2 Experimental Setup

During these measurements, the sample was located in the UHV with a base pressure of about 10^{-11} Torr. SHG was measured at several incidence angles and the fundamental was generated by unamplified Ti:Sapphire laser (120 fs, 76 MHz rep. rate and 200 mW average power) focused to a spot radius of about $30\mu m$. The polarization was controlled by a set of polarizers and half-wave plates. The azimuthal angle origin is along the [110] axis of the sample. A reference PMT was used to normalize SHG data against laser power variations. The RAS setup uses white light from a Xenon arc lamp. It is modulated by a PEM at 50 KHz. A schematic of the experimental setup can be seen in Fig. 2.13.

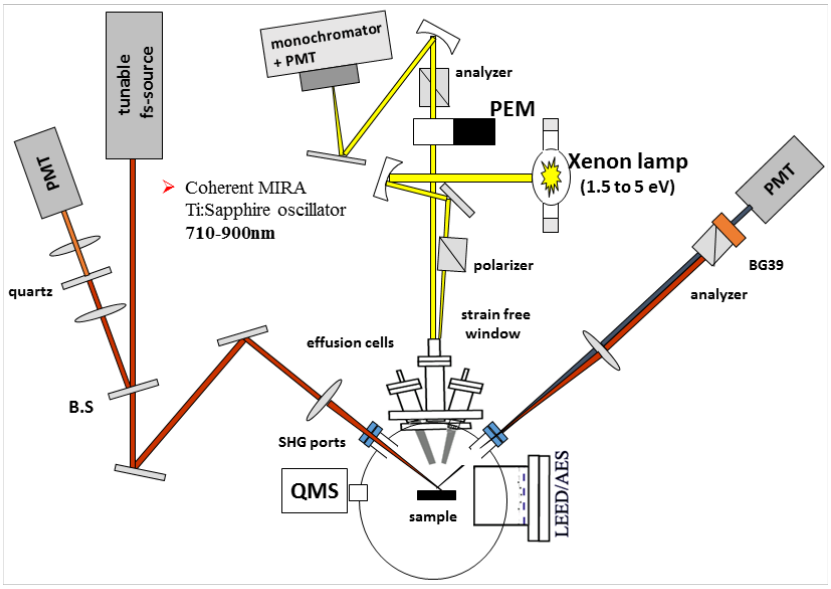

Figure 2.13: A schematic showing the major components of the experimental setup.

2.3.3 SHG of Clean and Hydrogenated Vicinal Si(001)

Following the process of achieving a clean, reconstructed Si(001) surface and injecting purified H_2 as described in Appendix A we measured SHG from a clean and hydrogenated vicinal Si(001) for sixteen different wavelentghs. We start our analysis by using Fourier decomposition. This work was taken from [1].

2.3.4 Fourier Decomposition of SHG

The SHG signal is analyzed using the phenomenologicall decomposition into the components of the Fourier sum 2.5. We can observe from Fig. 2.14 that with decreased wavelength the peack of the clean sample, at $\phi = 180°$ increases and develops a shoulder at $\phi = 100°$ and $\phi = 260°$ for $\lambda < 780nm$. The hydrogenated surface has significantly lower amplitude at $\phi = 0°$ and a clear shoulder at $\phi = 60°$ and $\phi = 300°$ with the peak decreasing for $\lambda < 780nm$ Using our data and previous studies [6, 62] we can infer that step edges contribute to all five components while terraces only weakly to a_1 and a_3 because of their tilt on the surface normal by the offcut angle. Back bonds were found to contribute to a_0 [63].

$$E_{p,p}^{(2\omega)} = \sum_{j=0}^{4} a_j^{p,p}(\omega) cos(n\phi) \tag{2.5}$$

The fits shown here, with all real coefficients excpet the complex a_0, are the best while minimizing the number of parameters and are shown in Fig. 2.15.

However it is easy to notice that we have only achieved an only peripheral

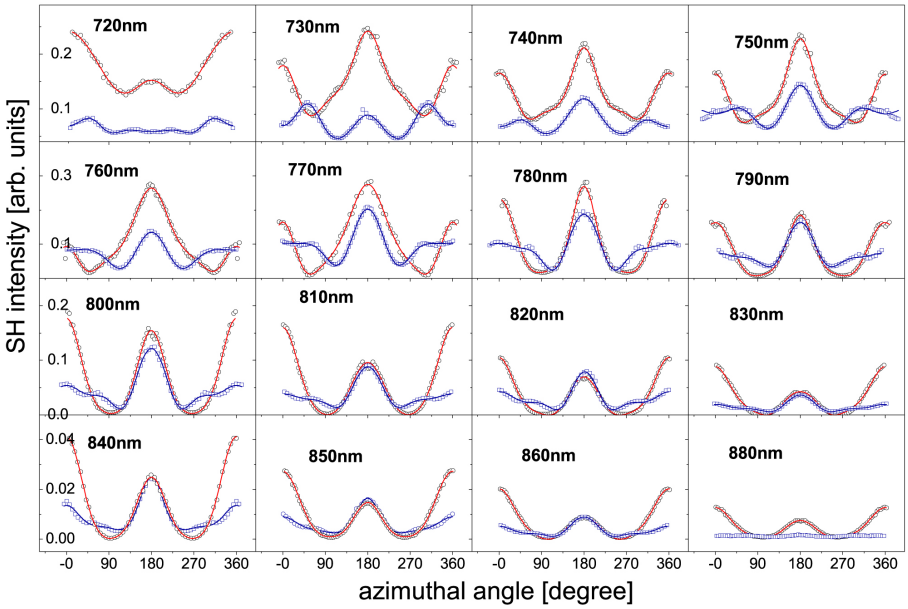

Figure 2.14: The SHG response, over an azimuthal sample rotation, for clean (open circles) and hydrogenated (open squares) Si(001):6°, for a spectrum covering our lasers spectral range, in a p-in/p-out geometry. The intensities are consistent only for each wavelength [1]. The solid curves represent fits using Fourier analysis with coefficients shown in Fig. 2.15.

connection to the true underlying physics. The knowledge of the spectral response of those parameters does not fully describe the SHG effect of each bond even with the RAS measurements not shown here. Furthermore we have six parameters constrained by sixteen different measurements once for clean and once for hydrogenated surface with differences not larger than the error bars in some cases. Also the fact that we have sixteen measurements means a time laboring experiment. Every measurement was approximately 15 minutes and it was performed twice once clockwise and another counterclockwise and for each wavelength we had to re-align the laser cavity and re-focus the focusing mirror thus taking about 40 minutes. Meanwhile the sample deteriorates significantly every 3 hours leading to the need to flash again, with the

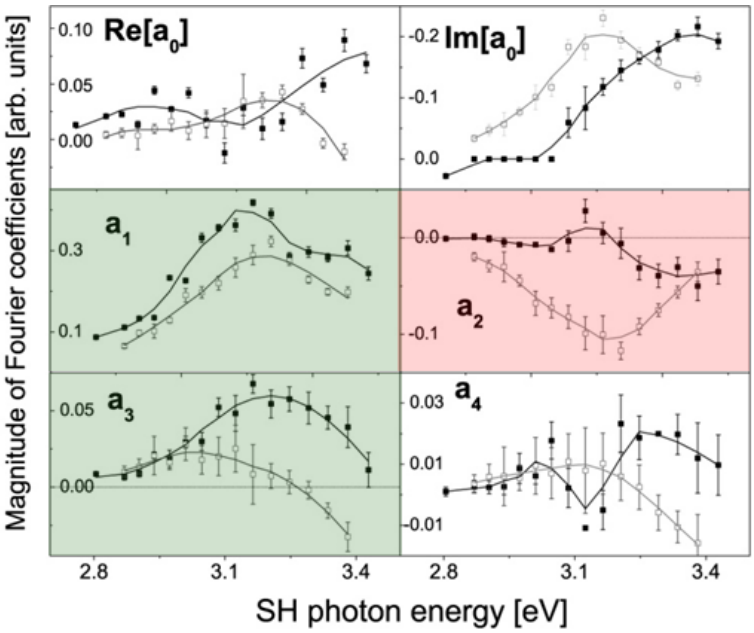

Figure 2.15: The spectra of the main Fourier coefficients from fitting SHG data in Fig. 2.14 for the clean surface (filled squares) and after exposure to molecular hydrogen (open squares) [1]. It is obvious that multiple parameters and assumptions are needed in order to understand the underlying physics using the conventional approach.

process taking about 5 minutes, and then some more time to restore vacuum. The subtle changes during those delays creep into our measurements, making the response SHG intensity not universally consistent.

Chapter Three: Optical Fingerprinting of Si(001) Bonds

In this chapter we present an improved and highly expandable version of SHG-MAP. We improve upon the earlier version by introducing an almost turn-key framework where bond and surface orientations (for suitable surfaces) can be used to computationally identify experimental geometries that would isolate the SHG response of individual bonds. The framework is modular with an SHG response generation stage and an fingerprinting identification stage. In the first stage the SHG response is calculated with or without Fresnel scaling for every possible parameter combination. In the second stage we can use a number independent fingerprinting identification algorithms.

The modular nature of this framework allows for any of its components to be improved without changes in the others: we can generate new SHG responses with improved bond orientations or keep altering the number of bonds. We can also use fingerprinting identification algorithms based on intensity or curvature. Another advantage is of course the computational nature of the framework which can identify fingerprinting geometries not initially obvious to the user in a matter of minutes.

Below we start by introducing the main components of SHG-MAP for each stage. We also present some of the major findings: predicting for the first time novel geometries for fingerprinting every bond of clean vicinal Si(001) without the

need for adsorbants and fingerprinting geometries for oxidized Si(111). Afterwards we demonstrate SHG-MAP by monitoring adsorption of atomic hydrogen and chemical etching of rebonded r-D_B and design a possible methodology to fingerprint the resulting dihydrogeneated surface.

3.1 Physical Represantation

3.1.1 Basic Assumptions

In order to predict the macroscopic second harmonic response of each bond a number of assumptions is made:

- The phase information is not included aka there is no contribution from the imaginary part.
- The bond is assumed to be a perfect dipole with motion restricted along the axis.
- The dangling bonds of down tilted atoms which are charge poor do not contribute.

The bonds are grouped in 6 groups according to their nature, location and orientation: step dangling bonds, terrace dangling bonds, rebond, dimer, step back bonds and terrace back bonds. As presented in previous chapters they have very different behaviors when it comes to chemical reactions but here it will also be shown that we

can also distinguish their second harmonic response based on purely monochromatic geometrical properties. We start by presenting the mathematical representation of each of the components in the SBHM equation as developed by Aspnes et al. [49].

$$\vec{E}_{p,p}^{(2\omega)} = \frac{k^2 e^{ikr}}{r}(\hat{I} - \hat{k}\hat{k}) \sum_j (\beta_{2j}^{\parallel} \hat{b}_j \hat{b}_j \hat{b}_j) \cdot \vec{E}\vec{E} \tag{3.1}$$

For simplicity the bond direction $\hat{b}_j$ will be represented as $\vec{B}$ in the rest of this chapter.

3.1.2 The Bond

Each bond can be considered as dipoles defined by the matrix

$$\vec{B} = \begin{pmatrix} cos\boldsymbol{\theta}.sin\boldsymbol{\gamma} \\ sin\boldsymbol{\theta}.sin\boldsymbol{\gamma} \\ cos\boldsymbol{\gamma} \end{pmatrix} \tag{3.2}$$

where $\boldsymbol{\theta}$ is the azimuthal angle (between the bond and $\hat{x}$) and $\boldsymbol{\gamma}$ the polar angle (between bond and $\hat{z}$).

The bond axes have to be rotated to the laboratory coordinates and this is achieved by applying an azimuthal rotation $R_z = R_a$ by an angle $\boldsymbol{\phi}$ (which is the same angle of rotation that we use in the lab when rotating the sample) and then a rotation $R_y = R_v$ by the vicinal angle (the small deviation of the sample structure from the major crystallographic axis) $\boldsymbol{\beta}$.

$$\vec{R} = \vec{R_y}\vec{R_z} = \begin{pmatrix} cos\boldsymbol{\beta} & 0 & sin\boldsymbol{\beta} \\ 0 & 1 & 0 \\ -sin\boldsymbol{\beta} & 0 & cos\boldsymbol{\beta} \end{pmatrix} \begin{pmatrix} cos\boldsymbol{\phi} & -sin\boldsymbol{\phi} & 0 \\ sin\boldsymbol{\phi} & cos\boldsymbol{\phi} & 0 \\ 0 & 0 & 1 \end{pmatrix} \tag{3.3}$$

To rotate the axis we use

$$\vec{R}^{\top} = \begin{pmatrix} cos\boldsymbol{\beta}.cos\boldsymbol{\phi} & sin\boldsymbol{\phi} & -sin\boldsymbol{\beta}.cos\boldsymbol{\phi} \\ -cos\boldsymbol{\beta}.sin\boldsymbol{\phi} & cos\boldsymbol{\phi} & sin\boldsymbol{\beta}.sin\boldsymbol{\phi} \\ sin\boldsymbol{\beta} & 0 & cos\boldsymbol{\beta} \end{pmatrix} \tag{3.4}$$

Applying this to the original bond we get the "rotated" bond:

$$\tilde{B} = \vec{R}^{\top}\vec{B} = \begin{pmatrix} \tilde{B_x} \\ \tilde{B_y} \\ \tilde{B_z} \end{pmatrix} = \begin{pmatrix} cos\boldsymbol{\beta}.cos\boldsymbol{\phi}.cos\boldsymbol{\theta}.sin\boldsymbol{\gamma} + sin\boldsymbol{\phi}.sin\boldsymbol{\theta}.sin\boldsymbol{\gamma} - cos\boldsymbol{\phi}.sin\boldsymbol{\beta}.cos\boldsymbol{\gamma} \\ -cos\boldsymbol{\beta}.sin\boldsymbol{\phi}.cos\boldsymbol{\theta}.sin\boldsymbol{\gamma} + cos\boldsymbol{\phi}.sin\boldsymbol{\theta}.sin\boldsymbol{\gamma} + sin\boldsymbol{\beta}.sin\boldsymbol{\phi}.cos\boldsymbol{\gamma} \\ sin\boldsymbol{\beta}.cos\boldsymbol{\theta}.sin\boldsymbol{\gamma} + cos\boldsymbol{\beta}.cos\boldsymbol{\gamma} \end{pmatrix} \tag{3.5}$$

3.1.3 Electric Fields

The incident electric field at an incidence angle $\boldsymbol{I}$ is assumed to have linear polarization with an angle $\boldsymbol{\Omega}$ from the p-polarization axis. So as an example:

- $\boldsymbol{\Omega} = 0$, p-polarization
- $\boldsymbol{\Omega} = 45$, q-polarization
- $\boldsymbol{\Omega} = 90$, s-polarization

$$\vec{E}(\boldsymbol{I},\boldsymbol{\Omega}) = \begin{pmatrix} -cos\boldsymbol{I}.cos\boldsymbol{\Omega} \\ sin\boldsymbol{\Omega} \\ sin\boldsymbol{I}.cos\boldsymbol{\Omega} \end{pmatrix} \tag{3.6}$$

The linear polarization of the incident electric field is one of the parameters we can control experimentally and thus one of the parameters of the fingerprinting technique.

We calculate the component $\hat{b}\hat{b} : \vec{E}\vec{E}$ as:

$$\vec{E}^{\top}\tilde{B}.\vec{E}^{\top}\tilde{B} = (E_x\tilde{B}_x + E_y\tilde{B}_y + E_z\tilde{B}_z)^2 \tag{3.7}$$

Although this component is dependent upon all the angles-parameters presented so far it contains no information about observation. That comes from the next component $\vec{C} = \hat{I} - \hat{k}\otimes\hat{k}$ where $\hat{I}$ is the three dimensional unitary matrix and $\hat{k}$ is the observation matrix:

$$\hat{k} = \begin{pmatrix} -sin\mathbf{V} \\ 0 \\ cos\mathbf{V} \end{pmatrix} \tag{3.8}$$

at the observation angle $\mathbf{V}$. The Kronecker product of the observation matrices is

$$\begin{pmatrix} -sin^2\mathbf{V} & 0 & -sin\mathbf{V}cos\mathbf{V} \\ 0 & 0 & 0 \\ -sin\mathbf{V}cos\mathbf{V} & 0 & -cos^2\mathbf{V} \end{pmatrix} \tag{3.9}$$

and it follows that:

$$\vec{C} = \begin{pmatrix} cos^2\mathbf{V} & 0 & sin\mathbf{V}cos\mathbf{V} \\ 0 & 1 & 0 \\ sin\mathbf{V}cos\mathbf{V} & 0 & sin^2\mathbf{V} \end{pmatrix} \tag{3.10}$$

3.1.4 Defining the $\hat{R}$ matrix

The $\vec{R}$ matrix define the second harmonic contribution of each bond according to the weight P and the terrace factor n.

$$\vec{R}_k = n_{s,t}.\sum_{i=1}^{t} P_i.\vec{E}^{\top}\tilde{B}_i.\vec{E}^{\top}\tilde{B}_i.\vec{D}_i \tag{3.11}$$

where n is 1 for step and 3 for terrace bonds, the sum is over the number of actual bonds of bond type i and $\vec{D}$ is:

$$\vec{D} = \vec{C}\tilde{B} = \begin{pmatrix} D_x \\ D_y \\ D_z \end{pmatrix} = \begin{pmatrix} cos^2\mathbf{V}.\tilde{B}_x + sin\mathbf{V}cos\mathbf{V}.\tilde{B}_z \\ \tilde{B}_y \\ sin^2\mathbf{V}.\tilde{B}_z + sin\mathbf{V}cos\mathbf{V}.\tilde{B}_x \end{pmatrix} \tag{3.12}$$

The total second harmonic field is then the sum for all bonds, for all tetrahedrons but for the dictionary we only take into account the real part for each individual bond type k :

$$\vec{E}_k(2\omega) = \begin{pmatrix} E_p(2\omega) \\ E_s(2\omega) \end{pmatrix} = \begin{pmatrix} \sqrt{R_{x,k}^2 + R_{z,k}^2} \\ R_{y,k} \end{pmatrix} \tag{3.13}$$

By applying a linear polarizer with axis of transmission at angle $\mathbf{\Omega}_{out}$ with the horizontal

$$\vec{A} = \begin{pmatrix} cos^2\mathbf{\Omega}_{out} & sin\mathbf{\Omega}_{out}cos\mathbf{\Omega}_{out} \\ sin\mathbf{\Omega}_{out}cos\mathbf{\Omega}_{out} & sin^2\mathbf{\Omega}_{out} \end{pmatrix} \tag{3.14}$$

which becomes $\begin{pmatrix} 1 & 0 \\ 0 & 0 \end{pmatrix}$ for $\mathbf{\Omega}_{out} = 0°$ (p-polarization), $\begin{pmatrix} 0.5 & 0.5 \\ 0.5 & 0.5 \end{pmatrix}$ for $\mathbf{\Omega}_{out} = 45°$ (q-

polarization) and $\begin{pmatrix} 0 & 0 \\ 0 & 1 \end{pmatrix}$ for $\mathbf{\Omega}_{out} = 90°$ (s-polarization). The general SHG signal after the analyzer at an angle $\mathbf{\Omega}_{out}$ with the horizontal is then given by

$$\vec{S} = \begin{pmatrix} S_1 \\ S_2 \end{pmatrix} = \begin{pmatrix} cos^2\mathbf{\Omega}_{out}E_p(2\omega) + sin\mathbf{\Omega}_{out}cos\mathbf{\Omega}_{out}E_s(2\omega) \\ sin\mathbf{\Omega}_{out}cos\mathbf{\Omega}_{out}E_p(2\omega) + sin^2\mathbf{\Omega}_{out}E_s(2\omega) \end{pmatrix} \tag{3.15}$$

To calculate the intensity $I(2\omega) = \vec{S}^{\dagger}.\vec{S} = S_1^2 + S_2^2$ since the electric fields are purely real. The expanded form of the SHG signal is then:

$$\begin{aligned} S\vec{H}G_k = &\left(cos^2\mathbf{\Omega}_{out}E_{p,k}(2\omega) + sin\mathbf{\Omega}_{out}cos\mathbf{\Omega}_{out}E_{s,k}(2\omega)\right)^2 + \\ &\left(sin\mathbf{\Omega}_{out}cos\mathbf{\Omega}_{out}E_{p,k}(2\omega) + sin^2\mathbf{\Omega}_{out}E_{s,k}(2\omega)\right)^2 \end{aligned} \tag{3.16}$$

which for $\mathbf{\Omega}_{out} = 0°$ (p-polarization) reduces to $S\vec{H}G_k = E_{p,k}^2$, for $\mathbf{\Omega}_{out} = 90°$ (s-polarization) it reduces to $S\vec{H}G_k = E_{s,k}^2$ and for $\mathbf{\Omega}_{out} = 45°$ (q-polarization) it reduces to $S\vec{H}G_k = \frac{1}{2}\left(E_{p,k} + E_{s,k}\right)^2$

3.1.5 Inclusion of Fresnel Factors

SBHM does not include the scaling of the electric field due to boundary conditions given by the generalized Fresnel factors. The expansion of the Fresnel factors to the nonlinear regime was introduced by Bloembergen et al. [54]. In a previous study with SBHM, only a single incidence angle was used, but, as we introduce the incidence angle as a free parameter, it is clear we need to introduce the appropriate Fresnel scaling. This is most obvious when comparing the SHG results of the

clean vicinal Si(001) surface to the individual bond responses for s_{in}/s_{out} polarization combination as seen in Fig. 3.1.

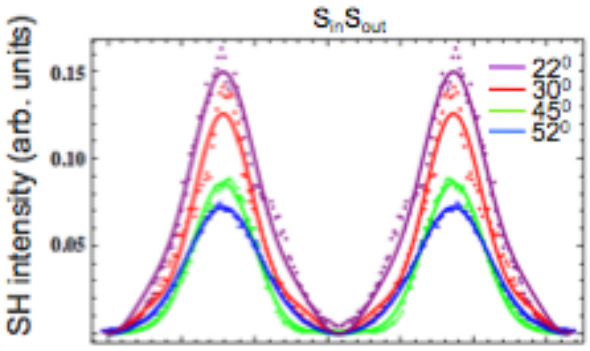

Figure 3.1: Fresnel scaling of intensity with incidence angle for major polarization combinations. Calculated SBHM intensities for different incidence angles do not show any such scaling when Fresnel factors are omitted [5].

In previous work [1, 5] where only p and s polarizations were used the nonlinear Fresnel factors were calculated following the work of Mizrah et al. [64] as shown in the following equations. For SHG from Si(001) in reflection, the transmission factors use the fundamental and the reflection factors, with the second harmonic dielectric constant $\epsilon = n^2$. The values are $n(\omega) = 3.7$ for 800nm and $n(2\omega) = 6.0$ for 400nm.

$$t_s = \frac{2cos(\boldsymbol{\theta})}{cos(\boldsymbol{\theta}) + \sqrt{\epsilon(\boldsymbol{\Omega}) - sin^2\boldsymbol{\theta}}} \tag{3.17}$$

$$t_p = \frac{2cos(\boldsymbol{\theta})\sqrt{\epsilon(\boldsymbol{\Omega})}}{cos(\boldsymbol{\theta})\epsilon(\boldsymbol{\Omega}) + \sqrt{\epsilon(\boldsymbol{\Omega}) - sin^2\boldsymbol{\theta}}} \tag{3.18}$$

$$r_s = \frac{cos(\boldsymbol{\theta}) - \sqrt{\epsilon(2\boldsymbol{\Omega}) - sin^2\boldsymbol{\theta}}}{cos(\boldsymbol{\theta}) + \sqrt{\epsilon(2\boldsymbol{\Omega}) - sin^2\boldsymbol{\theta}}} \tag{3.19}$$

$$r_p = \frac{cos(\boldsymbol{\theta})\epsilon(2\boldsymbol{\Omega}) - \sqrt{\epsilon(2\boldsymbol{\Omega}) - sin^2\boldsymbol{\theta}}}{cos(\boldsymbol{\theta})\epsilon(2\boldsymbol{\Omega}) + \sqrt{\epsilon(2\boldsymbol{\Omega}) - sin^2\boldsymbol{\theta}}} \tag{3.20}$$

For p-out the reflected SH efficiency is proportional to

$$I_{p_in or s_in} \propto tan^2\boldsymbol{\theta}[(1+R_p)t^2_{p_in or s_in}.E^2_{p,k} \tag{3.21}$$

and for s-out the reflected SH efficiency is proportional to

$$I_{p_in or s_in} \propto sec^2\boldsymbol{\theta}[(1+R_s)t^2_{p_in or s_in}.E^2_{s,k} \tag{3.22}$$

They predict a scaling in SHG intensity as seen in Fig. 3.2.

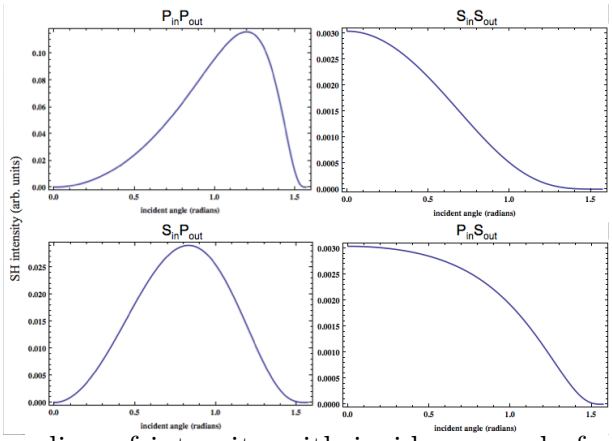

Figure 3.2: Fresnel scaling of intensity with incidence angle for major polarization combinations.

However, a more generalized approach is needed when the SHG-MAP is expanded to all polarization combinations. This is done by scaling the individual electric fields for each bond both in the incoming fundamental and observed second harmonic radiation. The Fresnel corrections for electric field is presented in Fig. 3.2. In previous work in our lab [1], the Fresnel corrected SBHM were used to fit results from clean, reconstructed vicinal Si(001) and fully H2-terminated Si(001) (1800L) at multiple incidence angles of 7.5°, 22°, 30°, 45°, and 52° show strong evidence for the inclusion of Fresnel factors as it is shown in Fig. 3.3.

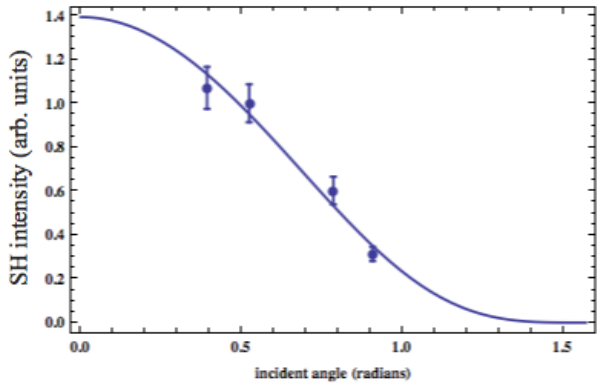

Figure 3.3: Fit using Fresnel factors for s_{in}/s_{out} polarization combination taken at an azimuthal angle of 90° on clean, reconstructed Si(001) [5]

3.1.6 Transmission and Reflection Coefficients

From the Fresnel Factors above we can calculate the transmission and reflection coefficients (where of course the interface is air - Si:

$$R_i = |r_i|^2 \tag{3.23}$$

$$T_i = \frac{\sqrt{\epsilon(\boldsymbol{\Omega}) - sin^2\boldsymbol{\theta}}}{cos\boldsymbol{\theta}}|t_i|^2 \tag{3.24}$$

where i denotes p or s polarization.

3.1.7 Scaling the electric fields

The incoming electric field has been defined as following:

$$\vec{E}(\boldsymbol{\theta}, \boldsymbol{\Omega}) = \begin{pmatrix} -cos\boldsymbol{\theta}.cos\boldsymbol{\zeta} \\ sin\boldsymbol{\zeta} \\ sin\boldsymbol{\theta}.cos\boldsymbol{\zeta} \end{pmatrix} = \begin{pmatrix} E_x \\ E_y \\ E_z \end{pmatrix} \tag{3.25}$$

where $\boldsymbol{\theta}$ the incidence angle and $\boldsymbol{\zeta}$ the polarization angle and it can also be transformed into a two component form:

$$\vec{E} = \begin{pmatrix} E_p \\ \\ E_s \end{pmatrix} = \begin{pmatrix} \sqrt{E_x^2 + E_z^2} \\ \\ E_y \end{pmatrix} \tag{3.26}$$

where it is trivial to apply the transmission coefficient for each component and then convert it back so we can use it directly into the SBHM:

$$\vec{E_F} = \begin{pmatrix} E_p T_p \\ \\ E_s T_s \end{pmatrix} => \vec{E_F} \begin{pmatrix} E_x T_p \\ \\ E_y T_s \\ \\ E_z T_p \end{pmatrix} \tag{3.27}$$

The same process can scale the SH electric field right before the analyzer is applied.

3.1.8 Orientation of bonds as input parameters

The polar and azimuthal angles defining the orientation of bonds are the input parameters in the SHG response generation stage. In terms of the other experimental parameters we assume that the incidence and reflection angles can take values from $0° - 90°$, as well as the incoming and outgoing polarization. The sample rotation angle can vary $0° - 360°$. These parameters are rotated to correspond to the actual surface of the material we are studying in which the bonds orientations are intrinsically defined.

From a structural and chemical affinity perspective the bonds can be separated into two main categories: bonds belonging to the **steps** of the staircase like structure

of vicinal silicon and the **terraces** as seen in Fig. 3.4. Not all the bonds presented in Table 3.1 for vicinal Si(001) are used in the calculations. Also as a reminder we assume only real hyperpolarizabilities for all bonds. The main assumptions are:

1. Only the charge-enriched Si dangling bonds of the **up-tilted** atoms of both **steps** and **terraces** are assigned P's (hyperpolarizabilities).

2. The back bonds of the upward and downward tilted dimers were assigned different P's due to asymmetry of the buckled dimers ($\beta_{back}^{terrace(up/down)}$).

3. The dangling bond orientations are the ones provided for hydrogenated surface from the literature.

4. For every pair of step bond unit we assume 3 pairs of asymmetric terrace dimers. Thus we can easily define an intensity difference in SHG repsonse over which the bond is consider "non-contributing".

5. The weak (compared to surface dipole SHG) quadrupole SHG from the bulk is not included.

The actual values used for bonds orientations of clean vicinal Si(100) are given in Table 3.2. The framework allows for any set of bond orientations to be entered here or these angles to be adjusted for further accuracy.

By using the table above and the pre-defined vicinal angle, we now have all the information needed to produce a complete table of possible SHG responses. The re-

Step Bonds (8)	
Rebond (2)	Up Down
Dangling (2)	Up Down
Back L (2)	Up Down
Back W (2)	Up Down

Terrace Bonds (16)		
Dangling (4)	Up	+Y
		-Y
	Down	+Y
		-Y
Dimer (4)	Up	+Y
		-Y
	Down	+Y
		-Y
Back L (4)	Up	+Y
		-Y
	Down	+Y
		-Y
Back W (4)	Up	+Y
		-Y
	Down	+Y
		-Y

Table 3.1: All the categories of bonds in the clean vicinal Si(001) surface.

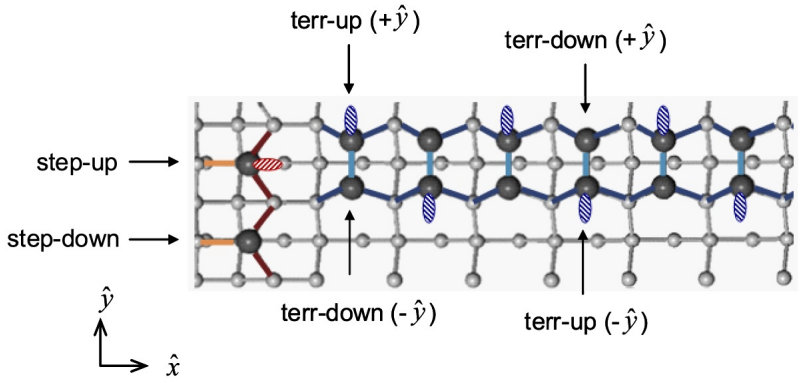

Figure 3.4: The bonds on clean vicinal Si(001) surface [2].

sponses are stored as comma separated values for easy retrieval. A sample is presented in Fig. 3.5.

These data can be used to graph the SHG responses for any bond and in any geometrical configuration. In Fig. 3.6 we plot the expected response (without Fresnel contributions) of the Terrace Back Bond for a sample rotation in a P-incidence and

Bond	γ	θ
Step Up Rebond	106.3	179.8
Step Up Dangling Bond	11.0	0
Step Up Back Bond L	55.2	114.9
Step Up Back Bond W	55.4	244.8
Step Down Back Bond L	73.3	117.1
Step Down Back Bond W	74.1	244.2
Terrace Up +Y Back Bond L	50	-18
Terrace Up +Y Back Bond W	60	-164
Terrace Down +Y Back Bond L	67	24
Terrace Down +Y Back Bond W	78	157
Terrace Up -Y Back Bond L	50	18
Terrace Up -Y Back Bond W	60	164
Terrace Down -Y Back Bond L	67	-24
Terrace Down -Y Back Bond W	78	-157
Terrace Up +Y Dangling Bond	13	90
Terrace Up -Y Dangling Bond	13	270
Terrace Up +Y Dimer	107	270
Terrace Up -Y Dimer	107	90

Table 3.2: The angles defining bond orientations for clean vicinal Si(001). These angle were provided by [6]

Incident Angle	Incident Polarization	Observation Polarizatior	Azimuthal Angle	Rebond	TerraceDB	StepDB	Dimer	StepB	TerraceB
0.6	0.8	0.9	4.7	0.172243	0.00349007	0.001867	0.006229	0.001009	2.2757
0.6	0.8	0.9	4.8	0.107691	0.00415423	0.001819	0.003364	0.000581	2.14178
0.6	0.8	0.9	4.9	0.06072	0.00517425	0.001755	0.000814	0.007631	1.96244
0.6	0.8	0.9	5	0.030197	0.00663213	0.001678	8.08E-05	0.022907	1.73791
0.6	0.8	0.9	5.1	0.012803	0.00862098	0.001591	0.002896	0.04367	1.47349
0.6	0.8	0.9	5.2	0.004377	0.0112345	0.001495	0.011005	0.064199	1.18103
0.6	0.8	0.9	5.3	0.001091	0.0145533	0.001394	0.025882	0.06513	0.879055
0.6	0.8	0.9	5.4	0.000159	0.0186294	0.001291	0.048419	0.022815	0.591158

Figure 3.5: A sample of the data table of the produced SHG responses with an increment of 0.1 radians.

P-detected polarization combination for three incidence angles. We can also start exploring other more unusual polarization combinations. In Fig. 3.7 we can see the expected results of the Rebond SHG response for three different incidence angles of 30°, 45° and 52° with P, S and Q polarization combinations. Q polarization is the results of the light polarization being exactly half in P and half in S polarization.

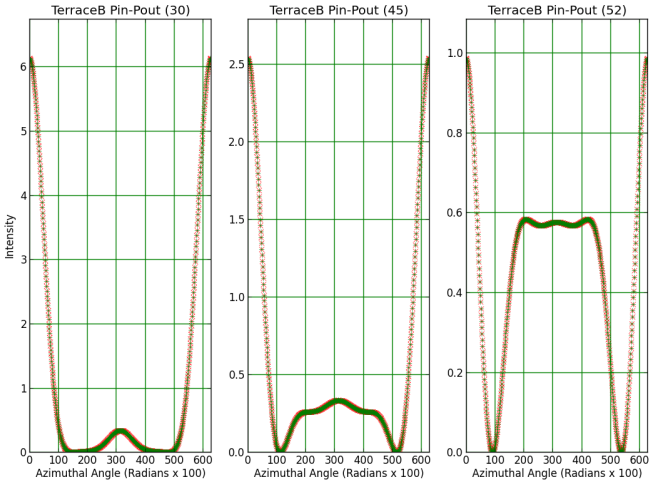

Figure 3.6: A sample of the produced SHG responses by sample rotation for Terrace Back Bond in incidence angles of 30°, 45° and 52° in a P-incidence and P-detected polarization combination.

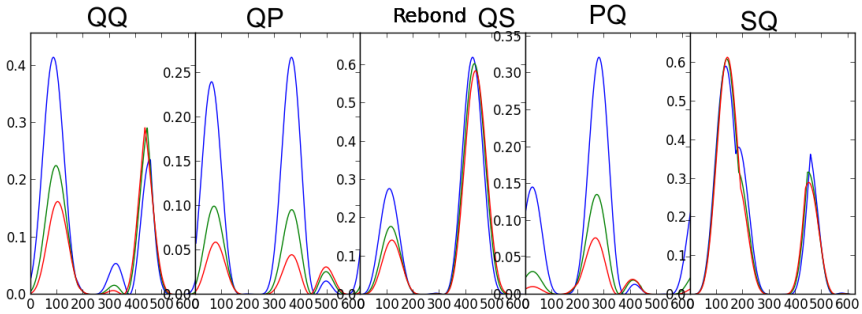

Figure 3.7: A sample of the produced SHG responses by sample rotation for the Rebond in incidence angles of 30°, 45° and 52° (red, green, blue respectively) in multiple polarization combinations of P,Q and polarizations.

The SHG response can also be plotted as three dimensional graphs by choosing to rotate over two of the input parameters. In Figs. 3.8 - 3.11 we plot the expected SHG response for each on of the bonds over incoming or observing polarization rotation and a sample azimuthal rotation for an incidence angle of 30°. From these we can definitely identify peaks and valleys for each bond and compare them in the hopes of identifying unique bond contributions for certain geometries. However it

become immediately obvious that such plots, although of a certain artistic value, are not particularly helpful in achieving fingerprinting. This was one of the major motivations for developing the fingerprint identification algorithm that is presented in the next section.

3.1.9 Rotating Polarization

We can easily allow for rotation of two parameters at once. Here we present the SHG response prediction for rotating the incoming or observed polarization during a sample rotation while keeping the observed or incidence polarization respectively on a fixed angle. In Fig. 3.8 we present the SHG responses over full rotation of the sample and the incoming polarization while observing P polarization for a clean vicinal Si(001) surface at a 30° incidence angle. In Fig. 3.9 we present the same results but for an S observed polarization. Alternatively in Fig. 3.10 we present the SHG response for a fixed S incidence polarization while rotating the observed polarization an sample and in Fig. 3.11 we can see the expected SHG response for a P incidence polarization.

Although these 3D graphs present a significant amount of information, it is hard to visually identify a geometrical configuration that will produce an SHG response originating from only on bond in all but the most simplest of cases. We solve this problem by developing a number of fingerprinting algorithms, presented in the next section, that will computationally isolate these geometries.

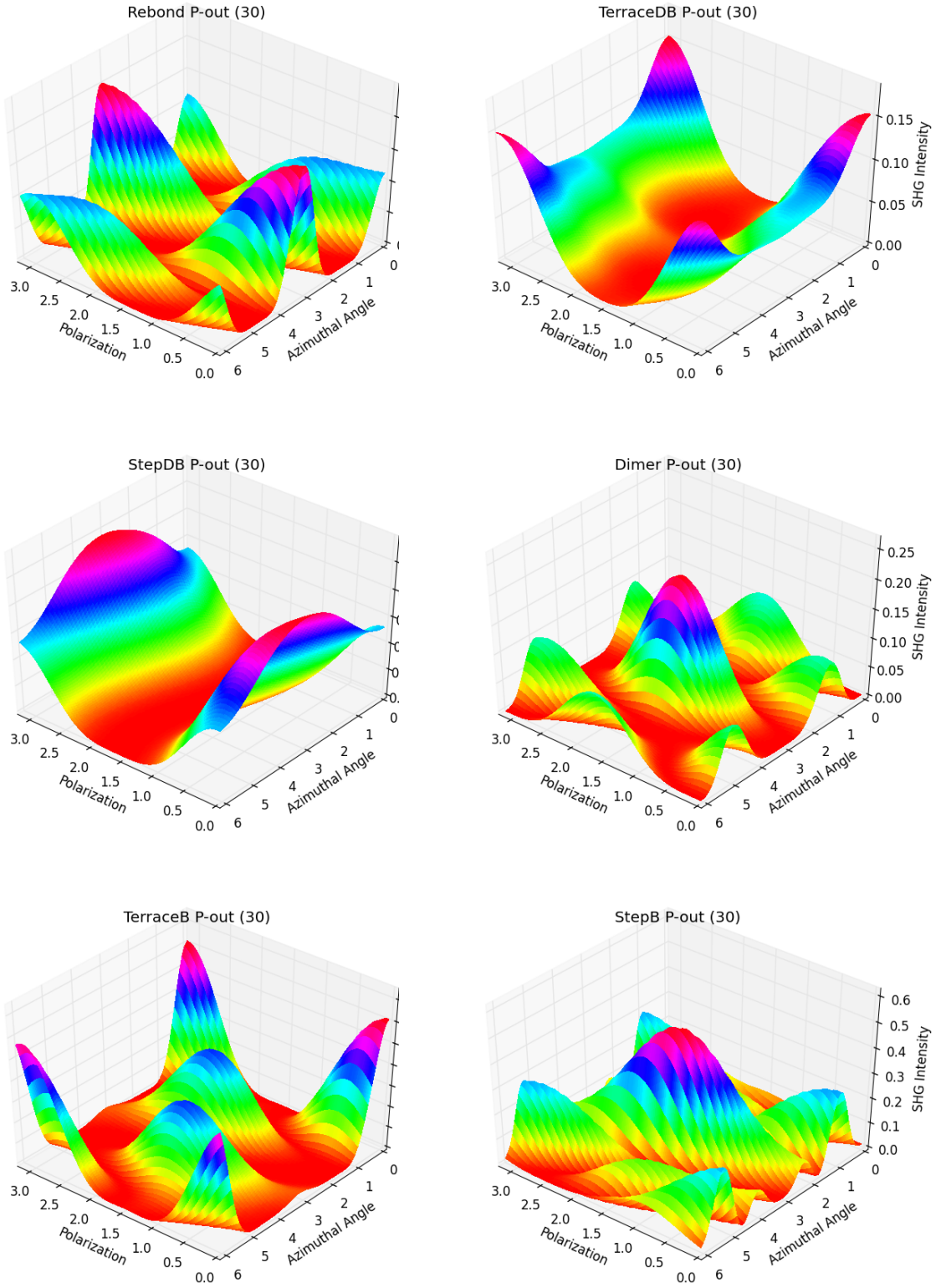

Figure 3.8: SHG responses over full rotation of the sample and the incoming polarization while observing P polarization for a clean vicinal Si(001) surface at a 30° incidence angle.

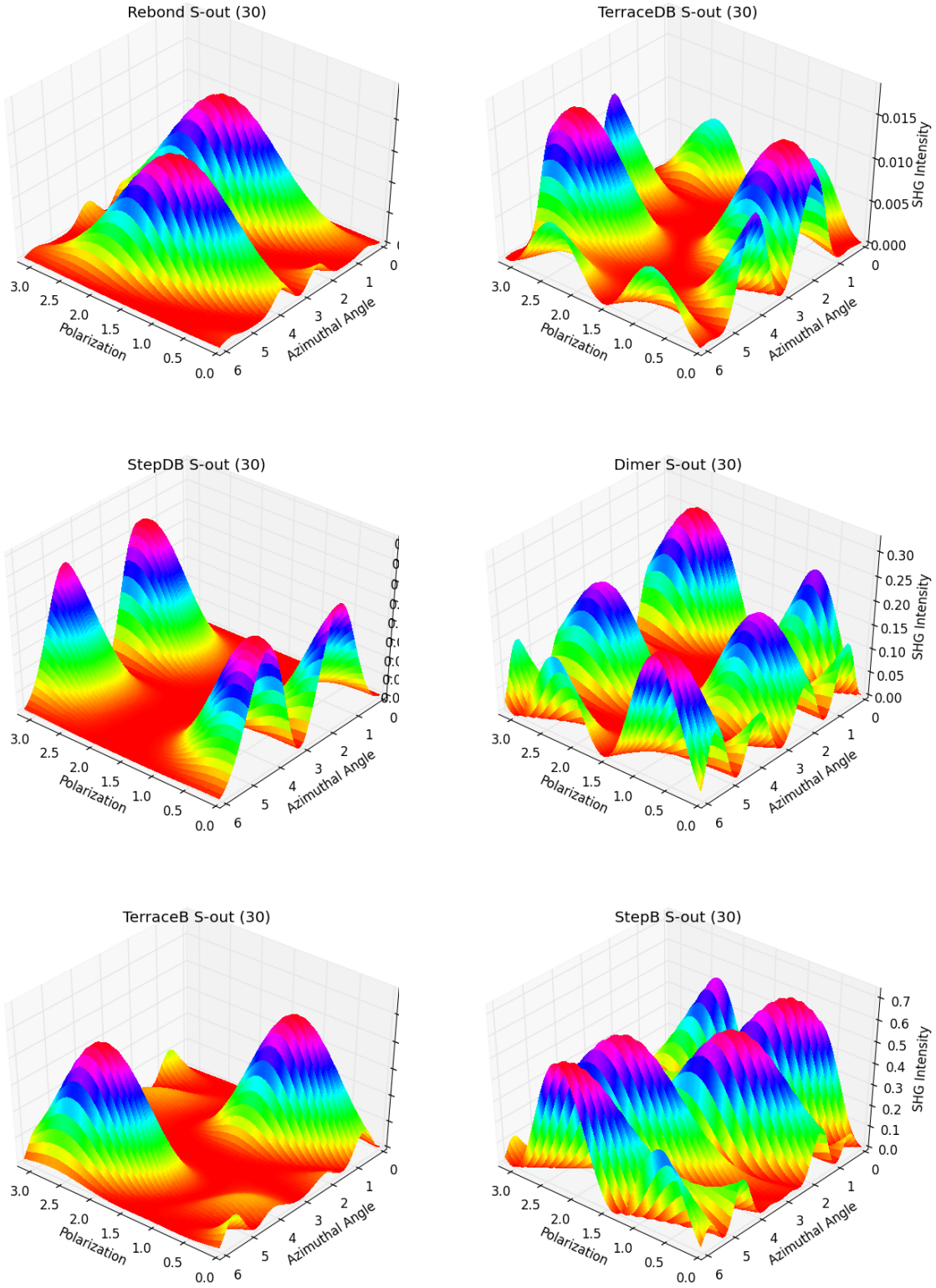

Figure 3.9: SHG responses over full rotation of the sample and the incoming polarization while observing S polarization for a clean vicinal Si(001) surface at a 30° incidence angle.

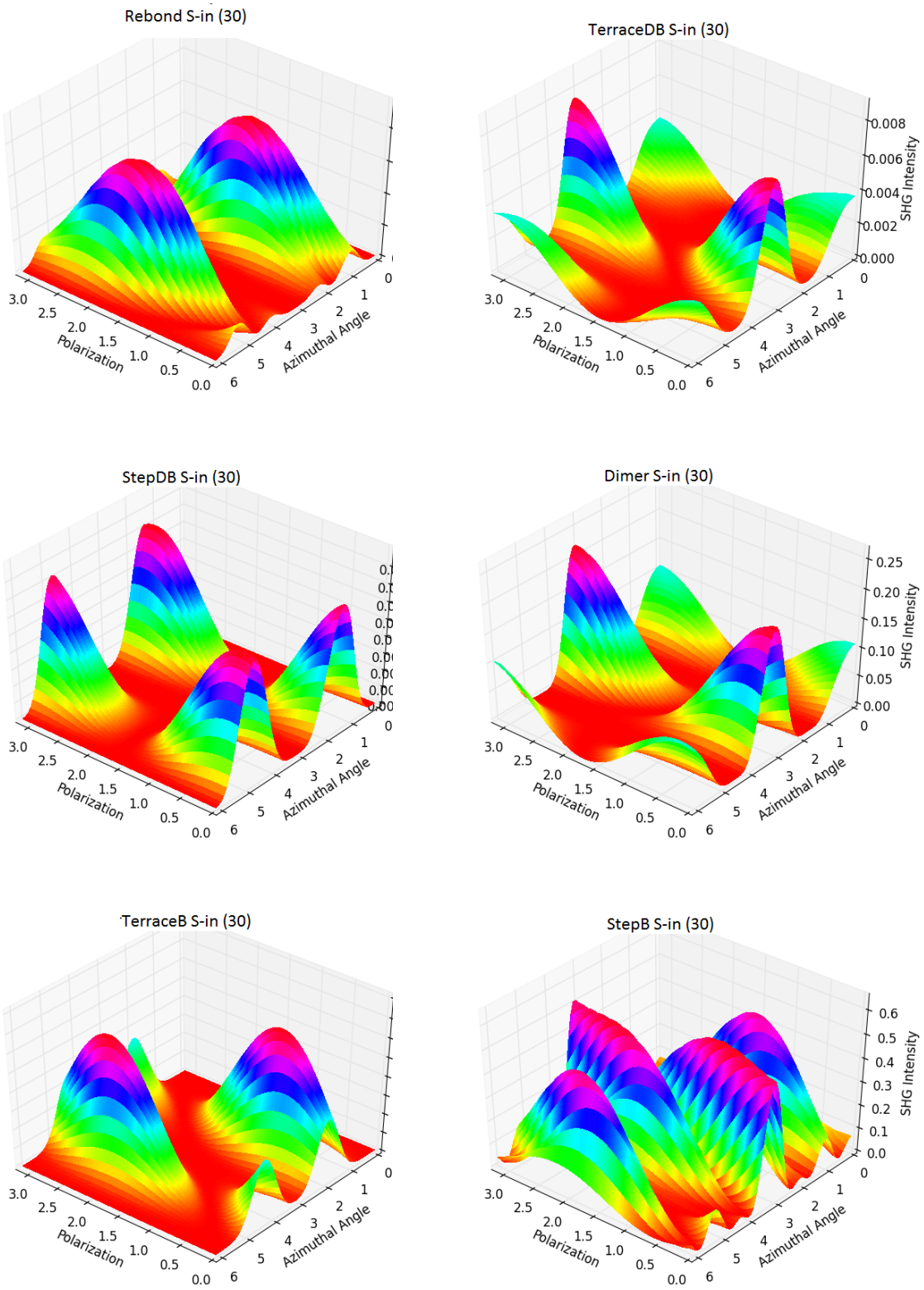

Figure 3.10: SHG responses over full rotation of the sample and the observed polarization whith incoming S polarization for a clean vicinal Si(001) surface at a 30° incidence angle.

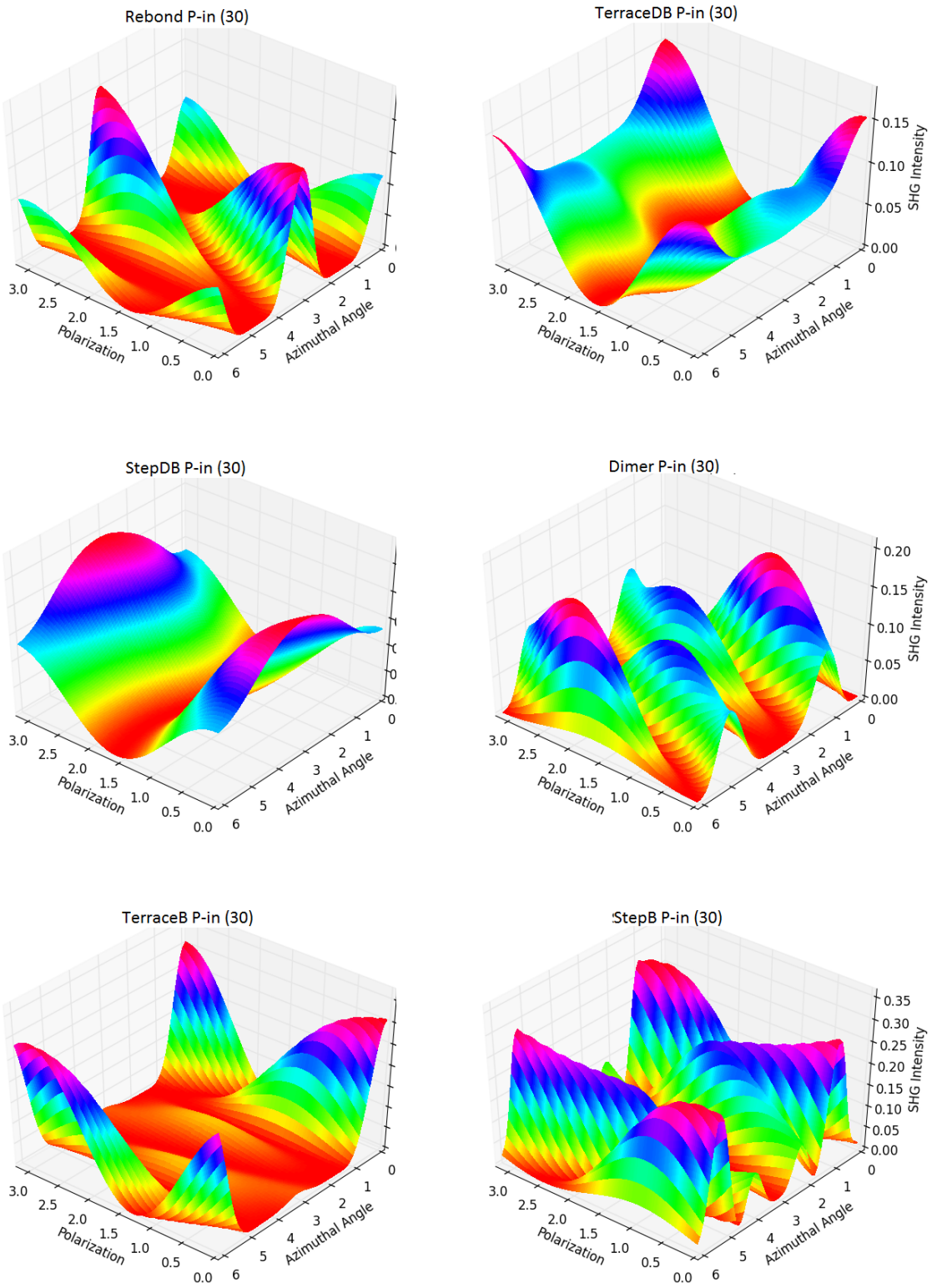

Figure 3.11: SHG responses over full rotation of the sample and the observed polarization whith incoming P polarization for a clean vicinal Si(001) surface at a 30° incidence angle.

3.2 Fingerprint Identification Algorithms

As mentioned above, the expansion of the SHG-MAP to include the SHG response of the full parameter space, creates the need for a more systematic method to identify unique bond contributions. The fingerprint detection algorithms presented below were developed by the author. The use of such algorithms has multiple benefits. Except providing a systematic method of fingerprinting, the reduce human effort, they provide more accurate results and mainly they can discover novel fingerprinting geometries. Lastly because of the modular nature of the framework, it is trivial to implement new and improved detection algorithms. Below we present the two main algorithms we use in this work: intensity fingerprinting and curvature fingerprinting.

3.2.1 Intensity Fingerprinting

The intensity fingerprint algorithm identifies experimental geometries where only one of the selected bonds contributes while all other bonds are practically not producing any SHG response. The process starts with the selection of a bond to fingerprint and the desired rotational parameter. The algorithm scans through all the other parameter configurations looking for intensity peaks along the selected rotational parameter. It uses a custom peak identifier developed by the author and based on Scientific Python (scipy) signal processing libraries to identify actual peaks. Then the width of that peak is defined along the rotational parameter by selecting the $\frac{1}{e}$ values of the current peak. Thus we create a list of peak centers and widths. This list

is then compared with the SHG responses of all other bonds and if they are practically non existent (around 3 orders of magnitude smaller)it is identified as a fingerprint. Then a six-fold two dimensional plot is created showing the proposed geometrical configuration and the expected SHG response along with the peak and width. The user can visually review this plot or filter the list of fingerprint configurations and images to correspond to the current experimental setup.

An example of such image for the clean vicinal Si(001) surface is shown in Fig. 3.12 as the prediction of the intensity fingerprinting algorithm for the Step Back bonds of clean vicinal Si(001) with the incidence angle as the rotational parameter without Fresnel contributions. Here it is proposed to use a very small incidence angle with 40.11° incoming polarization, P-observing polarization at a sample azimuthal angle of 91.67°. These values are always included as the title of the plot to avoid confusion.

3.2.2 Curvature Fingerprinting

The curvature fingerprinting algorithm identifies sharp peaks of bonds at locations where all other bonds have extremely wide peaks while taking into account the intensity. The same procedure is used as before but here the curvature κ of the peak of in the SHG intensity $I(x)$ is calculated where x is the rotational parameter. The curvature is calculated using Eg. 3.28:

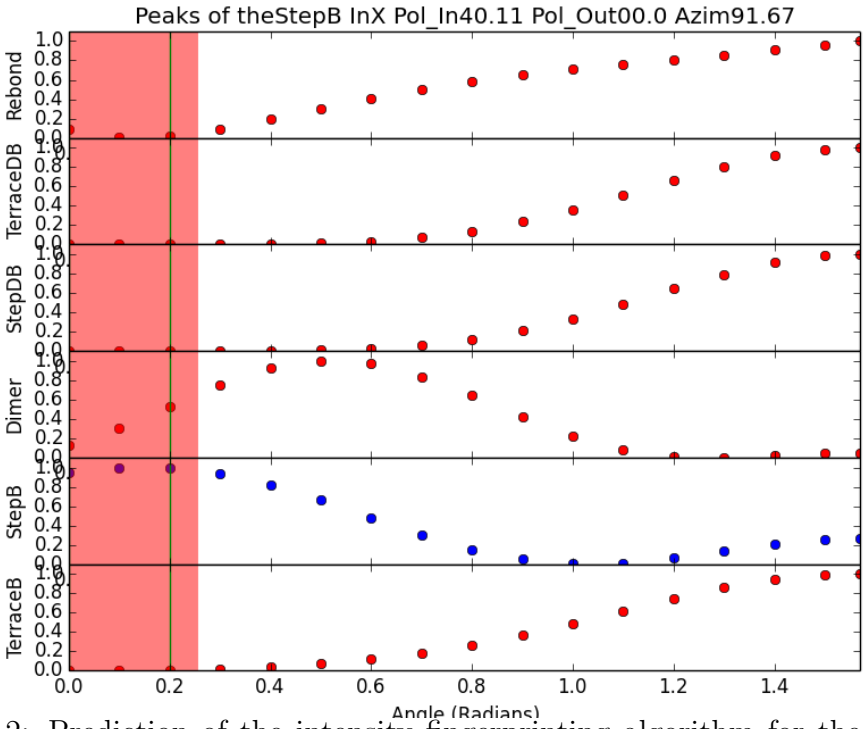

Figure 3.12: Prediction of the intensity fingerprinting algorithm for the Step Back bonds of clean vicinal Si(001) with the incidence angle as the rotational parameter without Fresnel contributions.

$$\kappa = \frac{|\ \frac{dI}{dx} + \frac{d^2I}{dx^2}\ |}{(\frac{dI}{dx})^3} \tag{3.28}$$

and compared to the local curvatures of all other bonds. Then, as before, a list of fingerprint candidates is generated along with plots to be reviewed by the user.

An example of such image for the clean vicinal Si(001) surface is shown in Fig. 3.13 as the prediction of the curvature fingerprinting algorithm for the Rebond of clean vicinal Si(001) with the sample azimuthal angle as the rotational parameter. Here it is proposed that at an azimuthal sample angle of around 60° with 11.46° incoming polarization, P-observing polarization at an incidence angle of 11.46° the

rebond peak will be sharper that other present peaks.

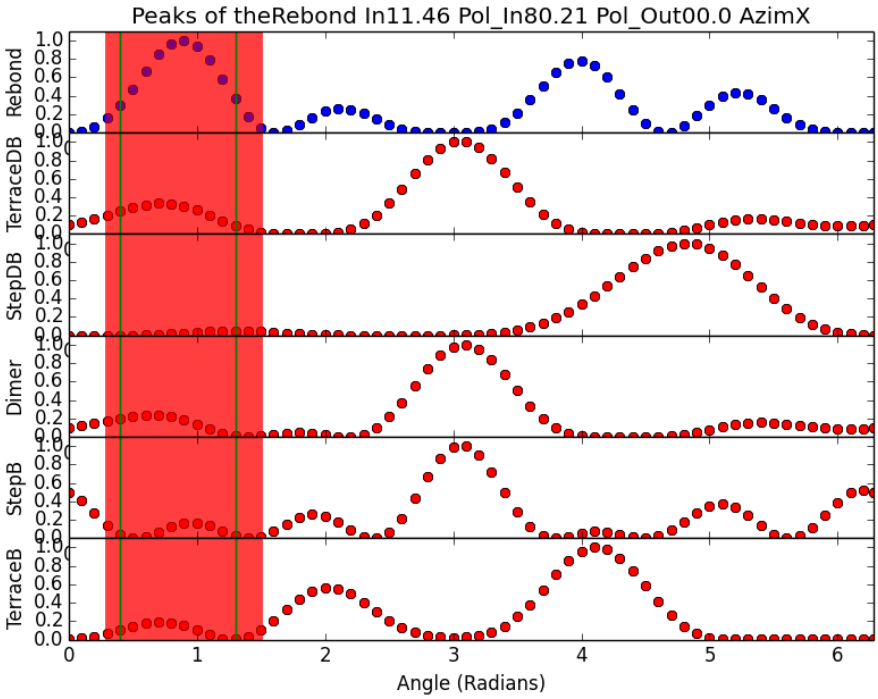

Figure 3.13: Prediction of the curvature fingerprinting algorithm for the Rebond of clean vicinal Si(001) with the sample azimuthal angle as the rotational parameter.

3.3 Applications and Predictions of the Fingeprinting Framework

Using the framework we developed we make predictions mainly using the clean Si(001) surface. Finally the framework is used for making prediction on a oxidized Si(111) surface.

3.3.1 Fingeprinting of clean vicinal Si(001) bonds

The immediate advantage of using the full parameter space and fingerprinting algorithms is that we can identify multiple fingerprinting geometries for each bond without the need to use adsorbants to passivate competing bonds. Below we present a collection of such fingerprints. Of course the experimental degree of difficulty varies wildly for these examples.

We start by presenting two examples for the Step Back bond in Fig. 3.14 and Fig. 3.15. In the first we can see an azimuthal rotation peak who is however really close to other peaks while in the second we see that we can fingerprint the Step Back bond using an almost perpendicular incidence angle.

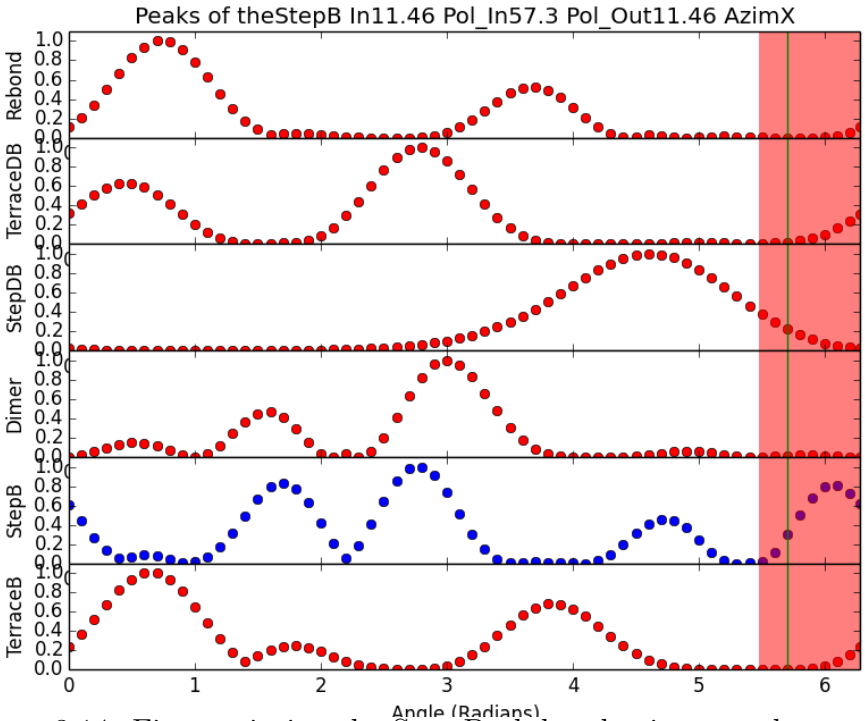

Figure 3.14: Fingerprinting the Step Back bond using sample rotation.

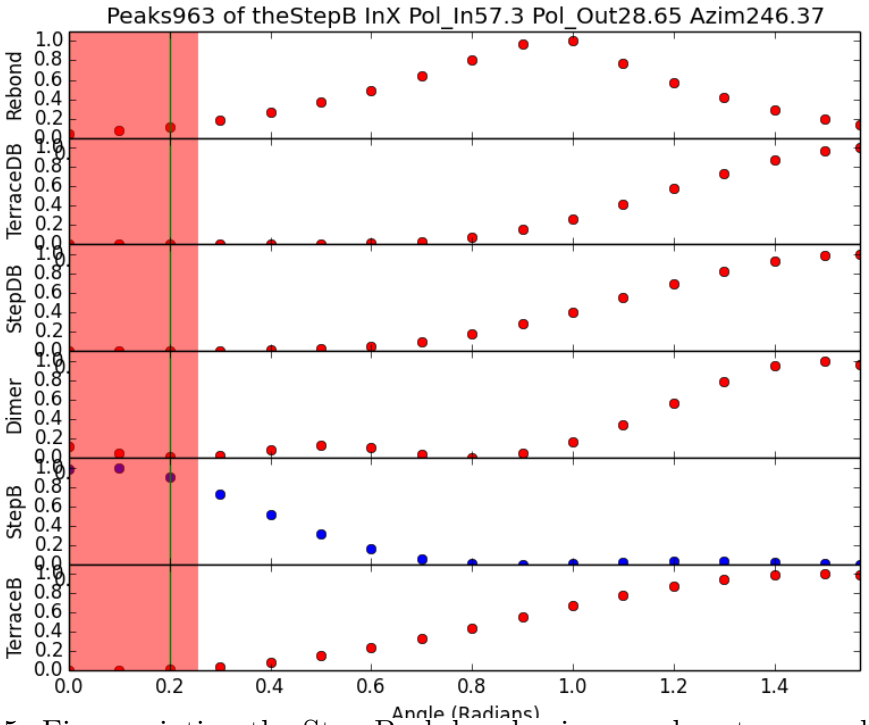

Figure 3.15: Fingerprinting the Step Back bond using an almost perpendicular incidence angle.

For the Dimer we can use another extreme incidence angle as seen in Fig. 3.16.

We showed an example of Rebond fingerprinting by sample rotation in a previous section. Here is an example of using a perpendicular incidence angle Fig. 3.17.

An experimental demonstration of fingerprinting, also published in [1], is to track the SHG response of the rebond during the introduction of molecular and atomic hydrogen. We use Fig. 3.18 to choose a suitable geometry.

We start by introducing around a million Langmuir of molecular hydrogen on the clean reconstructed surface to completely terminate [35] the step and terrace dangling bonds. It is known that in this dissociative adsorption the step dangling bonds will be terminated earlier [65] than the terrace dangling bonds [4, 28] but the

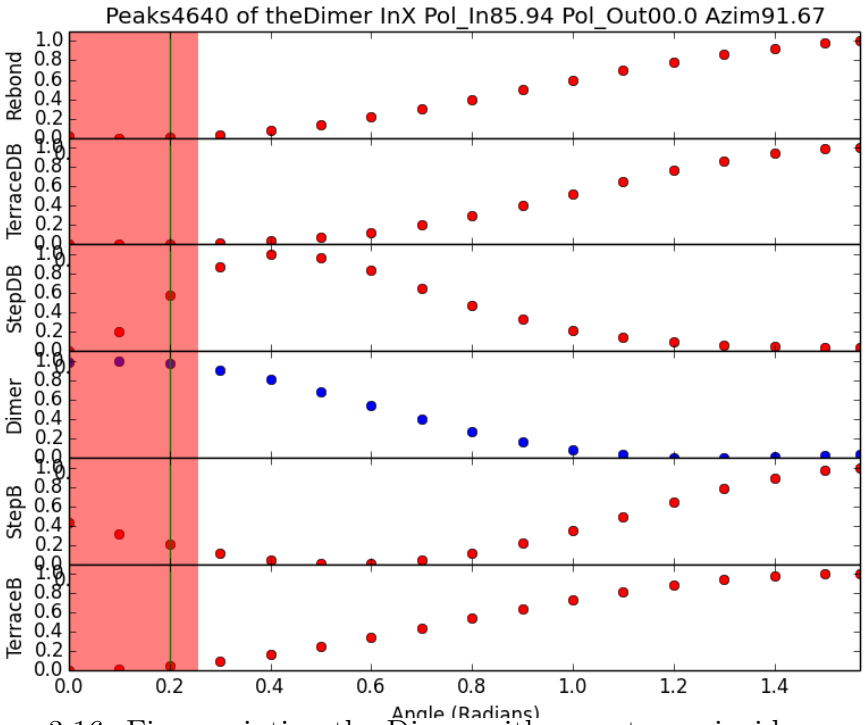

Figure 3.16: Fingerprinting the Dimer with an extreme incidence angle.

step rebond and the terrace dimers will remain intact. The introduction of atomic hydrogen at a dosage of 100 Langmuir shows the SHG response of the Rebond seen in Fig. 3.19, obvious from Fig. 3.18, is reduced because of the breaking of the Rebond by the atomic hydrogen as expected [3, 32, 66]. Introducing additional atomic hydrogen shows not only the rebond SHG reponse reducing but also the the SHG response associated with the terrace dimers at 1.5 and 4.8 radians.

For the Step Dangling Bonds we have two examples. In the first Fig. 3.20 we need to identify using curvature during sample rotation while it is "easier" to isolate if we can establish a grazing incidence angle as seen in Fig. 3.21.

For the Terrace Back bond we can use a rotation of the observed polarization

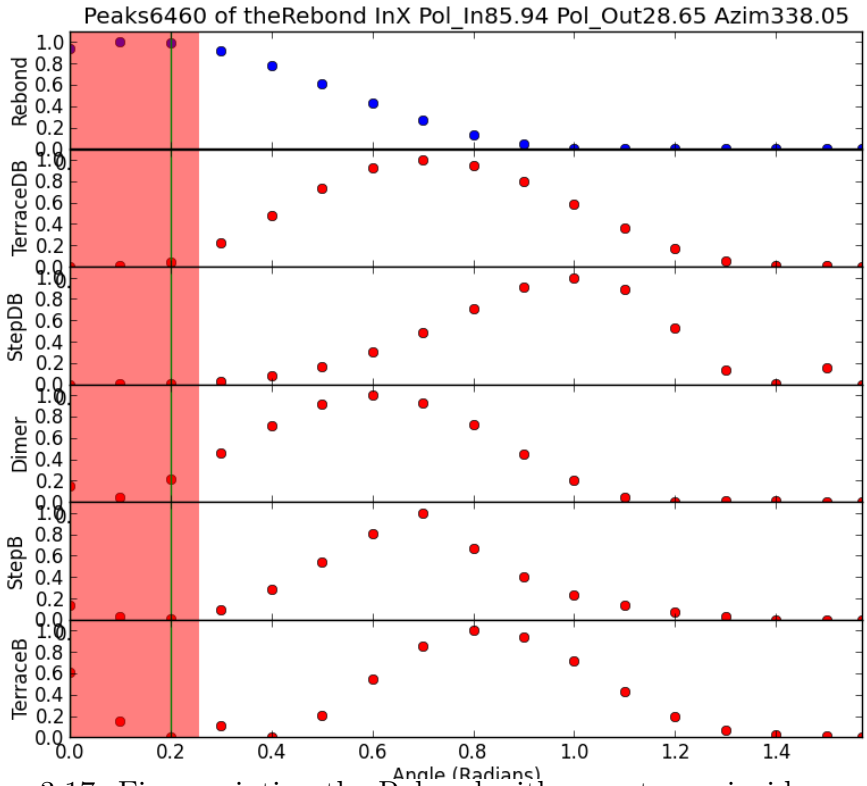

Figure 3.17: Fingerprinting the Rebond with an extreme incidence angle.

Fig. 3.22 while for Terrace Dangling Bond we can select a p incoming polarization as it can be seen in Fig. 3.23.

3.3.2 SiH_2 on a vicinal Si(001) surface

As we saw in the previous section by it is possible to break the terrace dimes by introducing atomic hydrogen achieve a dihydrogenated silicon surface. In order to propose an experiment to isolate the broken dimer bond SHG we need to re-visit the formation of the D_B surface. After removing the oxide the surface reconstructs by forming steps and buckling dimers,with rapidly switching orientations in room temperature, in order to reduce its surface energy. In our surface we see the formation

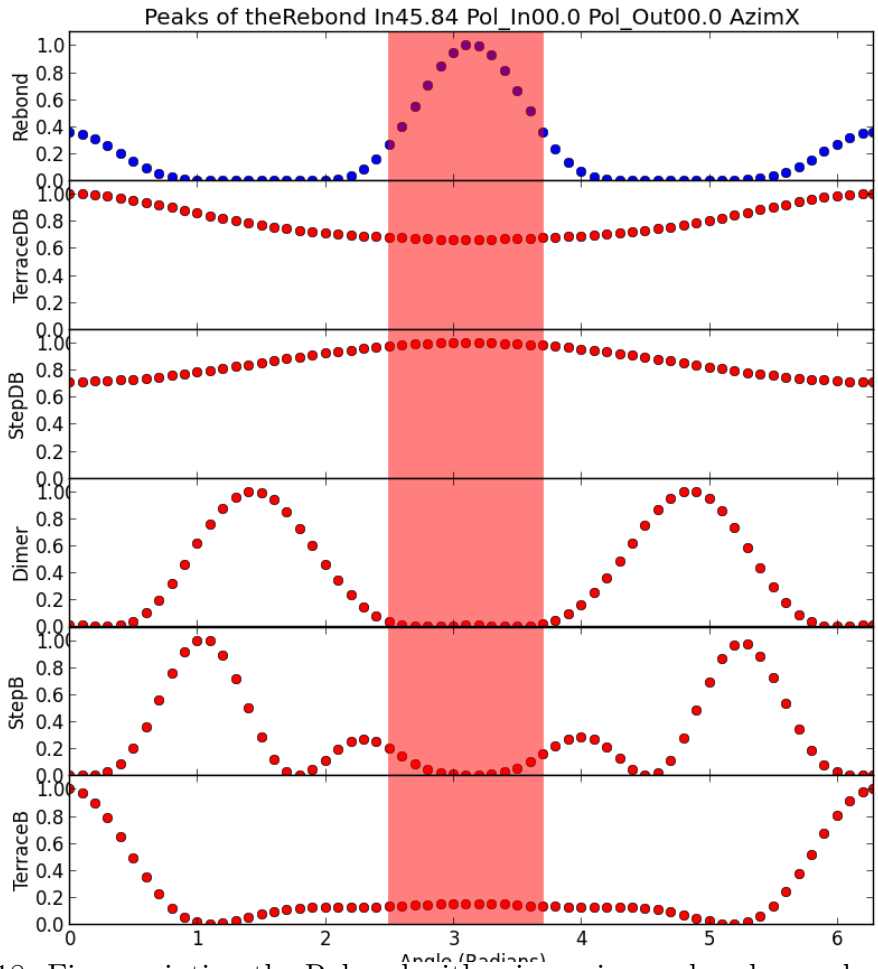

Figure 3.18: Fingerprinting the Rebond with p incoming and p observed polarization at an incidence angle of 45.84° with an azimuthal sample rotation.

of double steps and and the formation of a rebond at the step 2.6. The SHG response of the step bonds is generally higher from the terrace bonds and the asymmetry of the dimers is mitigated by their alternative buckling. When the step dangling bonds are terminated by molecular hydrogen [4, 35] the a charge transfer is observed from the charge rich dangling bond to the charge poor back bonds [1] and the buckling of the step dangling bonds dissipates. Similarly the terrace dangling bonds after termination transfer (in a lesser degree) charge to the back bonds, their buckling

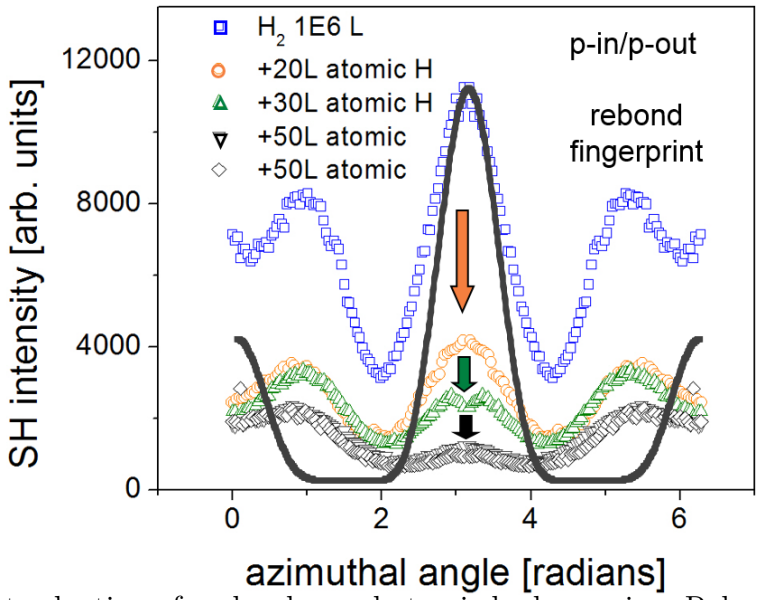

Figure 3.19: Introduction of molecular and atomic hydrogen in a Rebond fingerprinting geometry. We use p incoming and p observed polarization at an incidence angle of around 45° with an azimuthal sample rotation [1]. The solid line is the Rebond expected SHG response also seen in 3.18. We also notice that at 1.5 and 4.8 radians the SHG response is reduced.

dissipates as well as the buckling of their dimers. These leads to an even smaller SHG response from the dimers with an increased SHG response from the back bonds while the rebond response remains unchanged. The addition of $\alpha - H$ breaks the rebond [3, 32, 66] and the dimers completely after about 150 Lagmuirs as seen in 3.19 since we can safely assume that the back bonds do not interact. In a similar STM study, but with some key differences (temperature, no molecular hydrogen), Laracuente et al. [67] notes that the rebond is broken and they observed non-rebonded $n - D_B$ steps as well as non-rebonded single steps. This lead to a 3×1 structure around the step edges. The step edges remained intact as well as the terrace dimers. In the absence of other sources we can make some reasonable assumptions about the

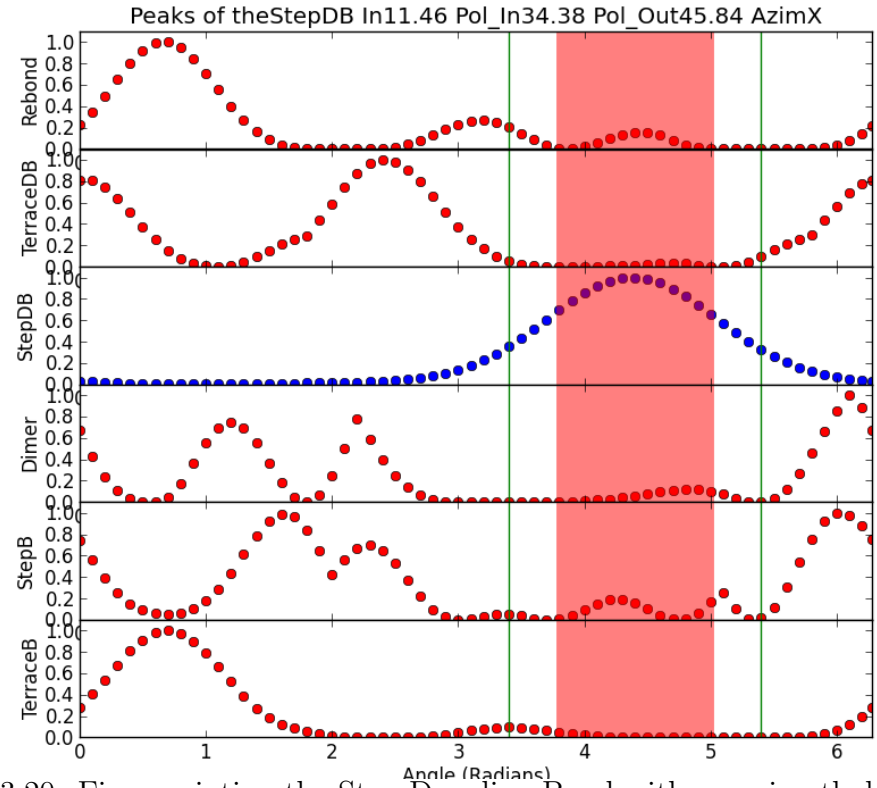

Figure 3.20: Fingerprinting the Step Dangling Bond with an azimuthal rotation.

state of our dihydrogenated surface: The lack of big changes in Fig. 3.19 and the SBHM predictions of 3.18 seem to indicate that all the rebonds and all the dimers are now broken and that the SHG at around 1.5 and 4.8 radians is due to the back bonds. Taking into account the STM observations (which do not fully correspond to our experimental conditions) we can assume that despite the dimers and the rebonds breaking and the dangling bonds fully terminated the overall structure of steps and terraces remains the same.

Of cource the broken bonds are now free to seek new orientations in order to reduce the surface energy. The new orientations as well as the change to a hydrogen - silicon bond both lead to a reduction of SHG reponse. With the information contained

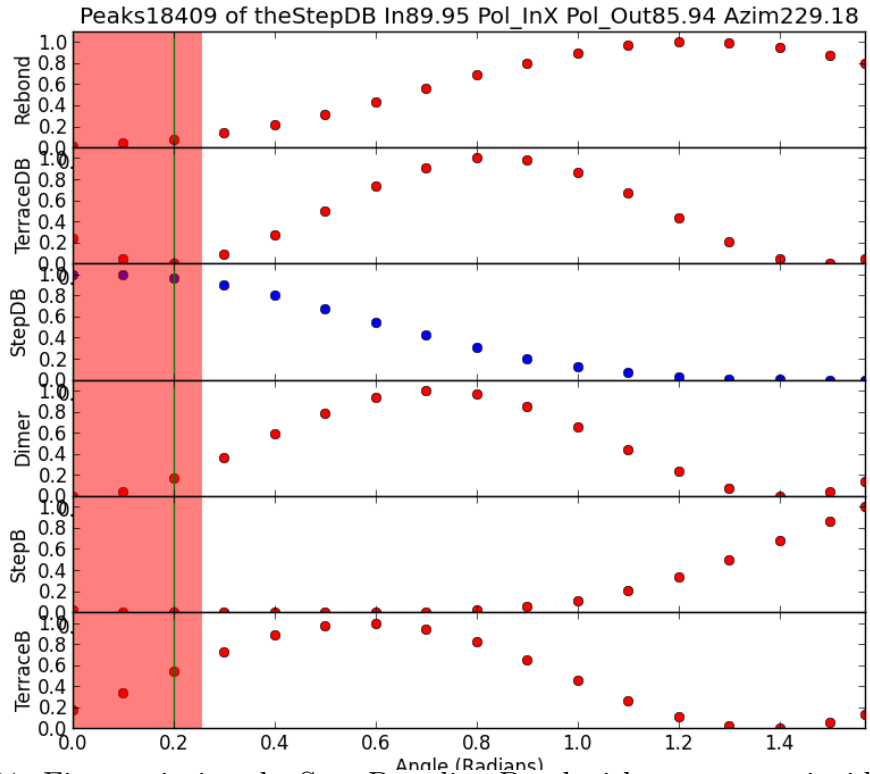

Figure 3.21: Fingerprinting the Step Dangling Bond with an extreme incidence angle.

in this work one can assume that the dimers and the rebonds Si-H bond will move away from the surface towards the dangling bond and away from each other in maybe a similar buckled fashion to maximize the distance from. In order to isolate the SHG response from the dimers we either need the new angles from ab-inition calculations or from STM obervations. Experimentally we could use one of the dangling bond orientations with a tilt towards the surface isolation geometries and head the surface in order to break the terrace dimer-hydrogen bond as it was observed.

For example in Fig. 3.24 the Terrace Dangling bond does not contribute and all the other competing bonds have been passivated. On could assume that a small but distinguishable SHG response from the broken dimer could be found there since

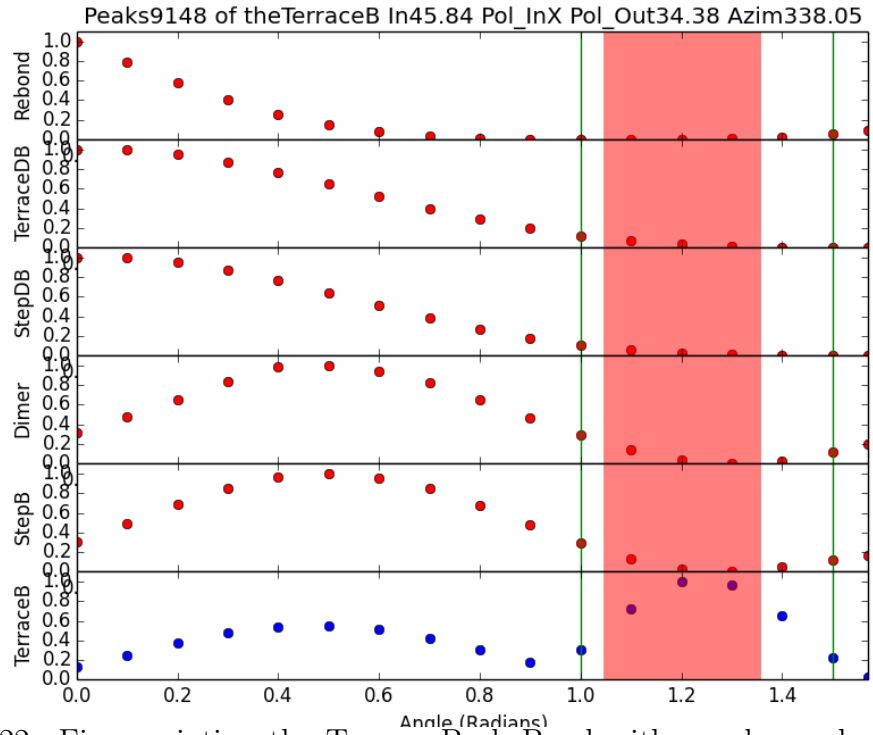

Figure 3.22: Fingerprinting the Terrace Back Bond with an observed polarization rotation.

it had peaks on either side.

3.3.3 Fingerprinting of oxidized Si(111) bonds

Clean vicinal Si(001) with a $2° - 6°$ offcut is a great candidate for SHG-MAP because of its distribution of bond orientations on the surface. Once exposed the atmosphere it quickly oxidizes producing a smooth Si/SiO_2 interface but with an almost random distribution of bond orientations at the interface. This is not the issue with oxidized Si(111), the atoms of the interface form a tilted tetrahedron with one atom almost perpendicular to the surface (not unlike the **"Dangling"** bond for clean vicinal silicon), two atoms acting as **"Back"** and another one we will name

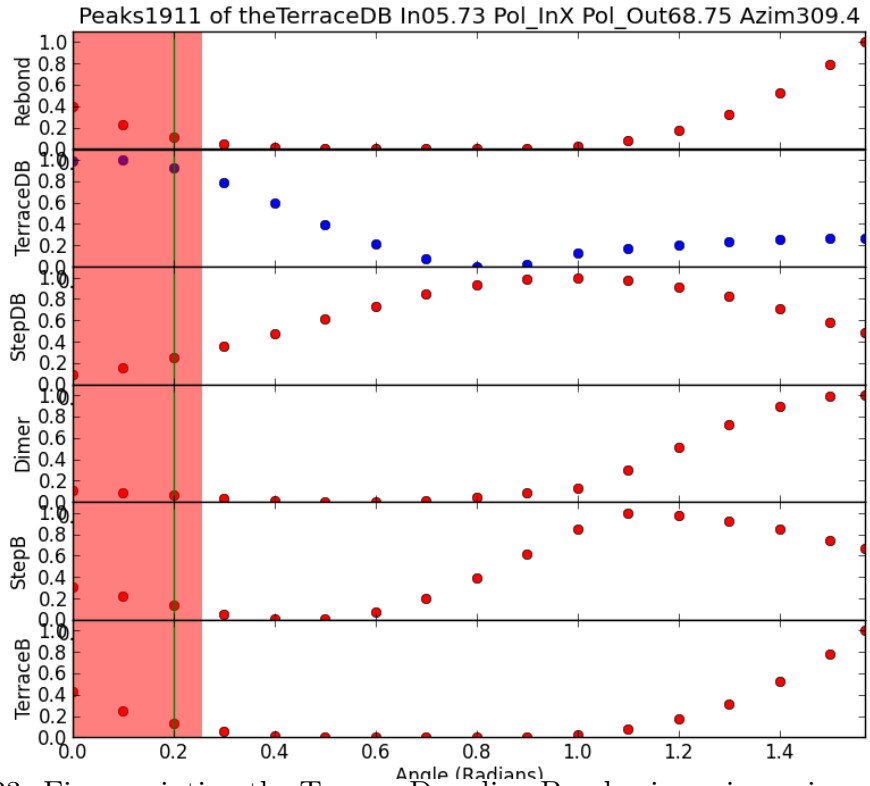

Figure 3.23: Fingerprinting the Terrace Dangling Bond using p incoming polarization

"Rebond" but does not actually act as one. These can be seen in Fig. 3.25 with the two **"Back"** bonds being the two symmetrical bonds towards the y direction. The bonds are provided by Dr. Onise Sharia who used a DFT model to match an amorphous SiO_2(111) to the Si(111) surface. The resulting angles are given in Table 3.3.

Bond	$\boldsymbol{\gamma}$	$\boldsymbol{\theta}$
"Rebond"	109.47	90.0
"Dangling Bond"	0.0	0.0
"Back Bond" 1	-109.47	60.0
"Back Bond" 2	109.47	60.0

Table 3.3: The angles defining bond orientations for the interface of Si/SiO_2. These angle were provided by Dr. Onise Sharia.

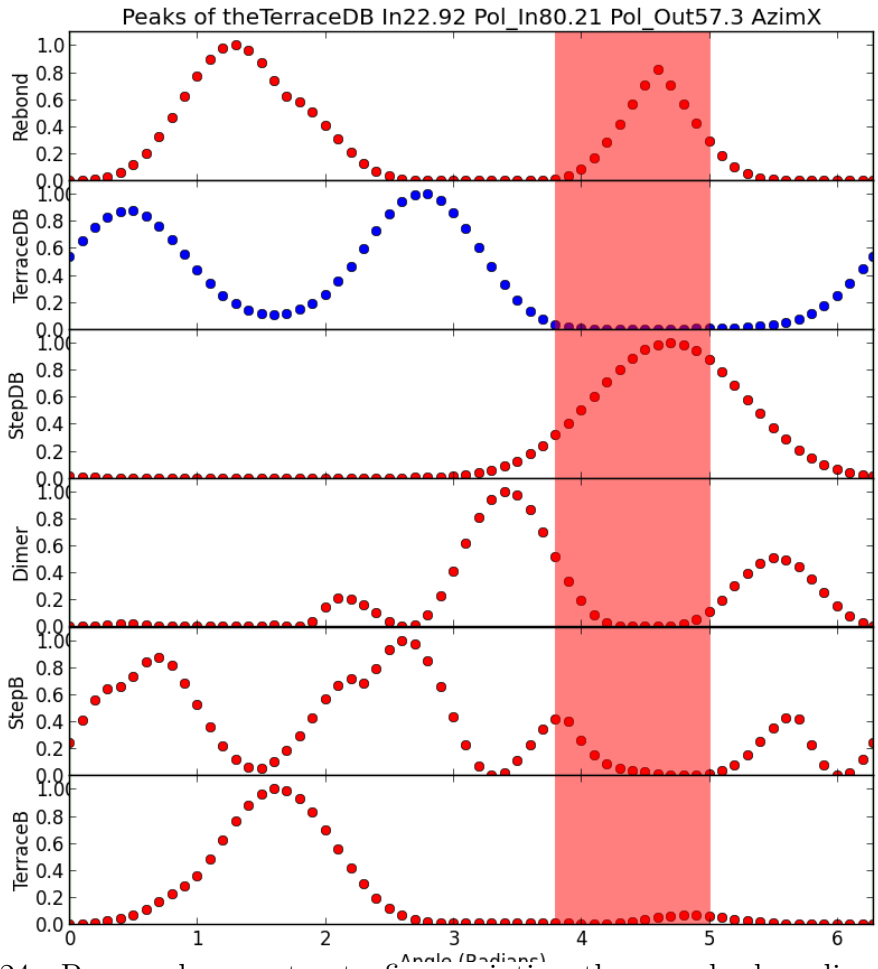

Figure 3.24: Proposed geometry to fingerprinting the now broken dimer by looking at location with everything that contributed has now been passivated and there shouldn't be any dangling bond SHG response. It uses an incidence angle of 22.92°, incoming polarization 80° and observing polarization 57° with a sample azimuthal rotation.

If we assume that the most of the SHG response is produce by these bonds at the interface we can identify some fingerprinting geometries to isolate those three bonds group : **"Dangling"**, **"Back"** and **"Rebond"**. In Fig. 3.26 we can see that there are more than one opportunities of fingerprinting the **"Back"** and **"Rebond"** bonds during a sample rotation even with using trivial polarization combinations. In

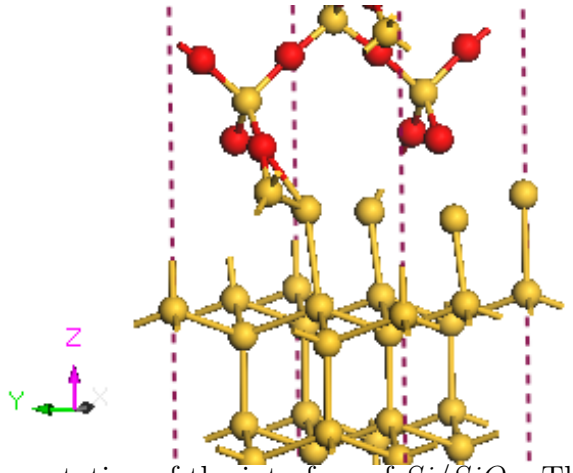

Figure 3.25: 3D representation of the interface of Si/SiO_2. The model was provided by Dr. Onise Sharia.

Fig. 3.27 we can see how choosing an extreme incidence angle can isolate the SHG response from the **"Dangling"** bond.

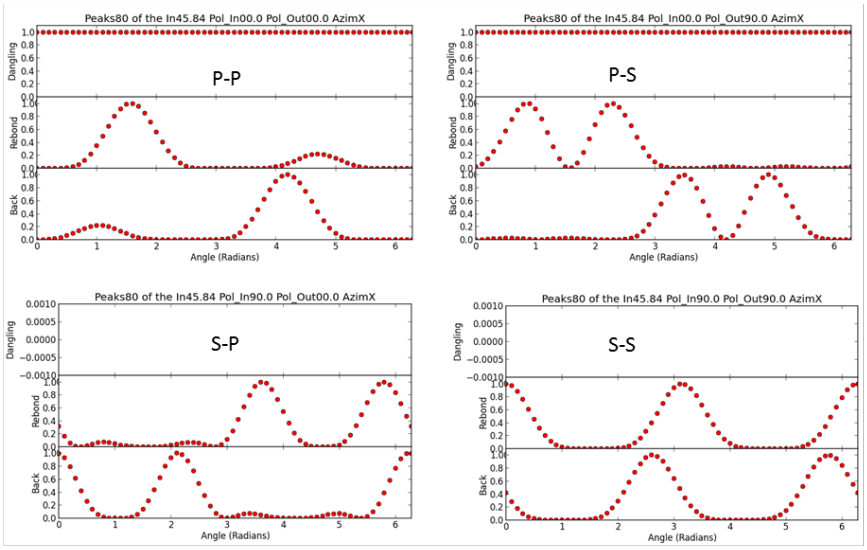

Figure 3.26: Fingerprinting the **"Back"** and **"Rebond"** bonds of the interface of Si/SiO_2 during a sample rotation with a combination of sample rotation and P or S incoming/observed polarization combinations at a 45.84° incidence angle.

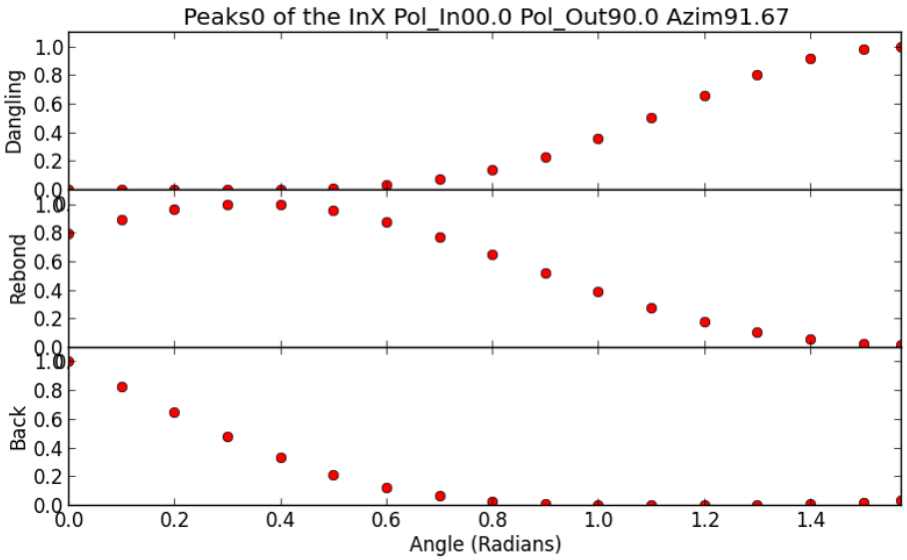

Figure 3.27: Fingerprinting the **"Dangling"** bond of the interface of Si/SiO_2 using an extreme incidence angle.

Chapter Four: Conclusions and Future of SHG-MAP

As we have seen in the previous chapters, fingerprinting using SHG-MAP can be a powerful monitoring method of the chemical activity of individual bonds under specific conditions. However, both in the SBHM and in SHG-MAP, we can propose changes to better connect with the underlying physical laws. Also in this chapter, we discuss other possible candidates for SHG-MAP.

4.1 SHG-MAP Improvements

4.1.1 Perpendicular charge motion

One of the assumptions of SBHM [30] was how the components of the hyperpolarizability tensor that were related with perpendicular charge motion were neglected. Allowing for the inclusion of those effects would significantly improve the quality of the predicted macroscopic SHG radiation thus providing more accurate fingerprinting results.

4.1.2 Fourth Harmonic Generation

The inclusion of the fourth order susceptibility $\chi^{(4)}$ can not only allow for the observation of higher order anisotropies [67] but also increase "resolution" of the fingerprinting technique and reveal new isolation geometries as seen in Fig. 4.1. Attempts to measure FHG from clean vicinal Si(001), using our current experimental setup, were not successful due to the low transmittance of the chamber optical windows which were bought to maximize transmittance around 400nm. A future study with appropriate windows is possible.

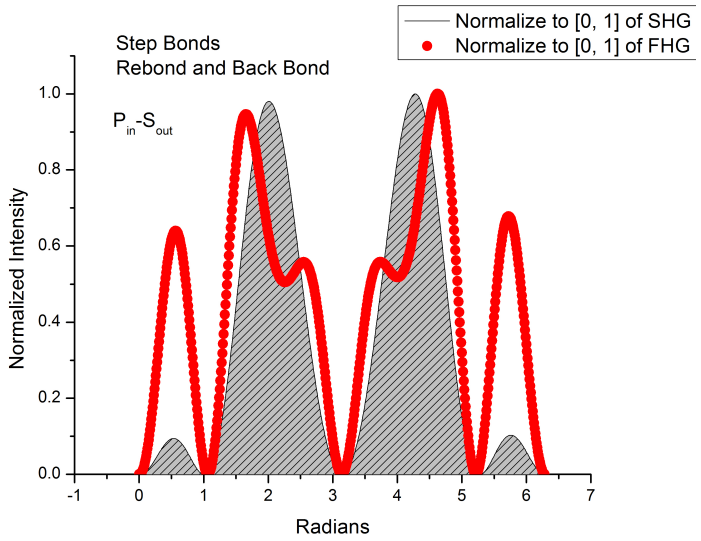

Figure 4.1: SBHM prediction for a combination of rebond and back bonds. We can see the increased resolution of FHG (red) versus SHG (grey), allowing us to distinguish the signal of each bond.

However, SBHM predictions for FHG were successfully used by Hardhienata [68] to model non-vicinal (111) diamond lattice results from earlier students of the Epioptics group [69].

4.1.3 Reverse Fingerprinting

The fingerprinting method is based on an "all but one" philosophy where only one of the bond groups contributes to the detected SHG. Exploration of the full parameter space has shown that we can also find geometries where "all except one" bonds contribute. This could be useful in the case of monitoring an adsorption process that is not meant to effect the detected bonds.

4.2 Future Experiments

4.2.1 Si(111)

As we discussed in Chapter 3, any single domain interface with clearly defined and somewhat distinct bond orientations may be a good candidate for applying the SHG-MAP method (as long as the bulk is not contributing to SHG). A perfect candidate is Si(111) which, due to its lattice structure, can easily be geometrically isolated and ab-initio DFT calculations can be obtained.

4.2.2 Strained Silicon

With the expansion of circuits, and especially FPGA, into the third dimensions through silicon via (TSV), configurations have become of interest and with them the effects of strain on silicon wafers. Both vicinal Si(001) ans Si(111) SHG-MAP predictions can be used to study strain especially when coupled with RAS.

Appendix A: Ultra High Vacuum Environment

The ultra high vacuum chamber was designed, purchased and built by Dr. Robert Ehlert as part of his dissertation [1]. He was aided by The University of Texas at Austin employees James Halligan, Donnie Carson, Allan Schroeder, Mike Ronalter, Jack Clifford, Ed Baez and Lanny Sandefur. Unfortunately a series of catastrophic events occurred in mid 2011 (turbo pump failures) until January 2012 (Robert Lee Moore Building power outage during Christmas break) forced a complete venting of the chamber, a gate valve replacement, turbo pump maintenance and a a series of restorative steps to restore UHV. Luckily I received the help of not only the people listed above but also from Dr. Watson Henderson and Dr. Rafal Zgadzaj in restoring the full functionality of the chamber.

A.1 Ultra High Vacuum Chamber

The UHV chamber is capable of maintaining a vacuum of 10^{-11} Torr measured with a filament based pressured monitor and checked using the QMS shown in A.1. The chamber is separated in three parts: the main chamber, the transfer arm and the gas/liquid injection arm. The main chamber is made from vacuum grade stainless steel. The chamber is cylindrical with about 30 cm in radius and approximately 120

cm in height. It allows for a sample to be positioned in approximately the middle with external manual controls for the xyz direction, while mechanized computer controlled azimuthal rotation is available. The translation system is located on the top of the chamber and connected to the chamber through bellows. As show in A.1, many laser beam appropriate optical ports are available. The RAS suitable strain-free optical port is located at normal incidence. The LEED is attached on the side of the chamber. The main chamber is pumped mainly by an ion pump with a titanium sublimination subsystem. It can only be operated once the vacuum is around 10^{-6} Torr.

To achieve the required pressure the chamber is initially pumped through the transfer arm and the injection arm. The transfer arm is connected to the main chamber through a gate valve which allows us to use the magnetically controlled "wobbling stick" to replace the sample without breaking vacuum. A turbo pump, backed by a mechanical rotary "backing" pump, is pumping the chamber at all times. The turbo pump can only be used after a pressure of 10^{-3} Torr has been achieved. The injection arm is also pumped by a combination of turbo and rotary pumps. It can be used to inject gases or liquids in the chamber. A cold trap is used to purify any liquids.

In order to achieve UHV, pumping alone is not enough. A thin film of water covers the walls of the chamber and pressure below 10^{-9} Torr cannot be achieved without heating up the chamber in a process called "backing". During this process the goal is to increase the desorption rate, mainly water from the walls of the chamber,

by heating the chamber to around 150° while pumping using only the turbo/rotary pumps. It is very important to avoid any cold spots where water can "hide" and heat the chamber uniformly to avoid cracking due to thermal expansion. Also, we need to remove all components that might be damaged from the heat. The chamber is wrapped in electric heating tape and the aluminum foil is used to constrain and evenly distribute the heat. Special care is taken to protect the optical windows from scratches while we slowly increase the temperature over a couple of days. In Fig. A.2 we can see the chamber wrapped up with electric heating tape and aluminum foil. After the baking is over all the filaments are operated in "degass" mode, and the titanium sublimination pump is used mainly to remove hydrogen.

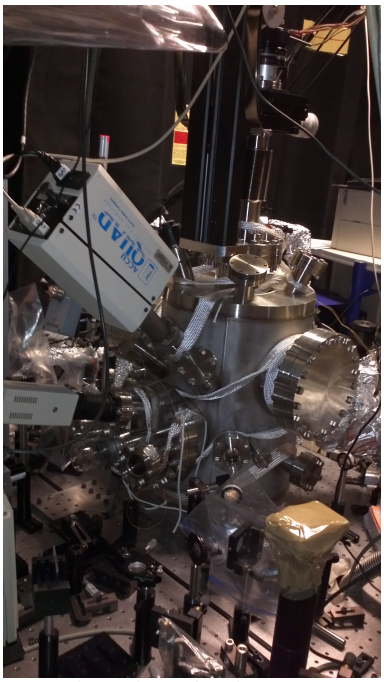

Figure A.1: The ultra high vacuum chamber.

Name	Manufacturer	Serial	Description
HPT-WX	VG Scienta	SE195883	Sample Manipulator
		MWXZ1515	Manual Wide Bore Z slide Module
		MRXXY12	HPT Precision Manual XY Module
		MR2R	Variable Length Rotary Drive Module
LN2 cooling	VG Scienta		
		ZLN	Liquid Nitrogen Cooling Module
		ZLNHX	Liquid Nitrogen Cooling Accessory Kit
	Omicron	B001966	LEED/Auger package
		B001955	4 grid SPECTALEED
		B001960	Electronics and software for LEED and Auger
		B000014	LaB6 filament
Sample stage	Omicron		RH1C
		B001329	Resistive sample heating facility
		B001331	Upgrade for direct heating current
		B001333	Sample transfer head
MLRM2	VG Scienta		Magnetically coupled transfer arm
	Bomco	B5936	Strain-free ultra high vacuum window
	MPF Products	A0650-1-CF	Laser entrance window
	MDC	ULV 150	Precision leak valve
PID	Eurotherm		Temperature controller
UHV-24	Varian		Nude Bayard-Alpert type
TCP 380	Balzer/Pfeiffer		Turbomolecular pump
CFV Turbo5051	Alcatel		Turbomolecular pump
VacIon Plus StarCell 150	Varian		ion pump + TSP
RGA 200D	Kurt Lesker		Residual Gas Analyzer

Table A.1: Major components of the ultra high vacuum chamber.

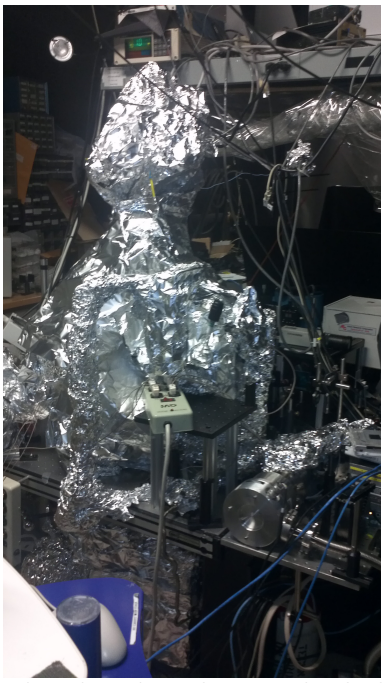

Figure A.2: The chamber during the baking process.

A.2 Low Energy Electron Diffraction

The LEED used in our experiment was SPECTALEED by Omicron. More information is shown in Table A.1. In Fig. A.3 the electron gun and phosphorus screen attached on the chamber is shown. The low energy electron gun is located on the side of our UHV chamber and the beam incidence angle range is partly defined by its location since we can rotate the sample to face it.

The electron beam is produced by a tungsten filament operated at 2500°C or a LaB_6 crystal at 1000°C. Early electron guns had beam energy widths of 0.3 eV and 0.1 eV respectively, but the one used here produces electrons with kinetic energies in the 10 - 200 eV range. Fig. A.4 shows a schematic of the gun and the three grids. The beam first passes from a negatively biased (up to 30V) electrode G1 or Wehnelt.

The Wehnel cylinder is a charged topless, hollow cylinder with a gap for the electron beam. The beam then passes through two more positively biased anodes (1 to 30 kV) that collimate and focus the beam. The focus is prefixed at around 20-30 cm from the LEED energy range so the sample is positioned close to the gun.

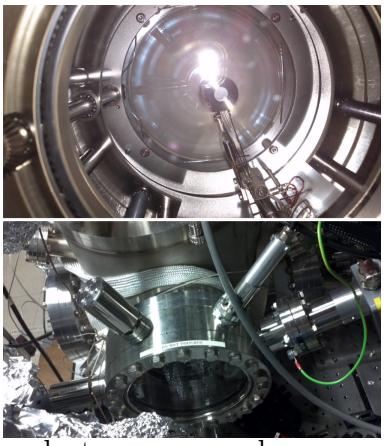

Figure A.3: The low energy electron gun and screen on the top image and their location on the chamber in the bottom image

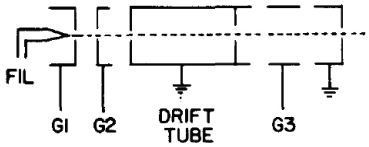

Figure A.4: An electron gun with the three grids that control the intensity and focus of the electron beam.

In Fig. A.5 we can see a diagram of a LEED system. A small percentage of the incident electrons will backscatter towards the screen or the detector, losing different amounts of energy. Before hitting the screen or the detector, the electrons that were backscattered from the sample have to go through three grids. The first two G1 and G2 in Fig. A.5 are negatively biased so only electrons that have lost less than 1-2 eV of their initial energy can go through. This is an effective way of

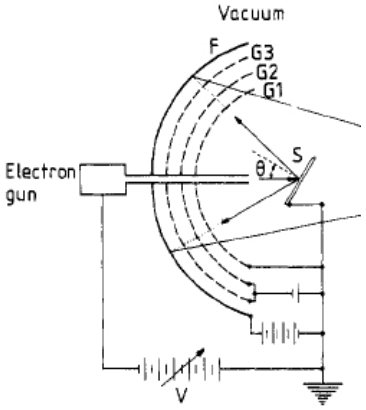

Figure A.5: Diagram of a LEED system featuring the screen with the three grids. G1 an G2 create a negative bias to filter out the inelastic scattered electrons while G3 is the post-acceleration grid which provides the electrons the sufficient energy to excite the phosphorus screen

selecting only the elastically scattered electrons, which is just 2-5 percent of the total amount of backscattered electrons [70]. The third grid, G3, is positively biased of the order of 1-2 eV and it provides the electrons with the energy to sufficiently excite the phosphorus screen. This is the process known as post-acceleration . For measuring the intensity of the spots, detectors such as a Faraday cup or the more modern and precise electron multiplier is used.

In order to use LEED to investigate surface structures it is important to first understand the results from well known surfaces and to then proceed into the investigation of surfaces with unknown structures. The LEED results can be qualitative or quantitative. The diffraction pattern is the main way of obtaining qualitative results. The spot positions are recorded and can be used in the size, symmetry and rotational alignment of the adsorbates with respect to the surface unit cell. It is important to

recognize that there are multiple structures that can be deduced from the diffraction patterns.

A.3 Sample Preparation and Adsorbate Introduction

In order to achieve a clean reconstructed Si(001) surface, we anneal the sample overnight at about 600° C. The samples are vicinal Si(001) with offcut angles of 4°, 6°, and 8° towards [110]. The backside of the wafer has been etched and coated with a conductive metal to allow for resistive annealing using lower voltages. The procedure, developed by Hata et al. [57], proceeds with flashing the sample to 1050° C for 30s using resistive heating in order to remove the oxide, as it is shown in Fig. A.6. The pressure remained in the 10^{-10} Torr range.

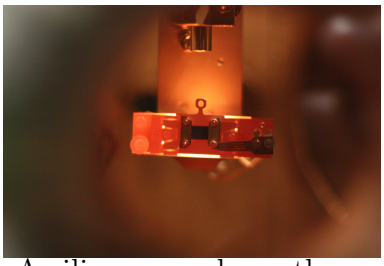

Figure A.6: A silicon sample on the sample holder

The resulting surface is dominated by double atomic height steps with three-fold coordinated Si atoms attached to the step edges (r-D_B steps) with terraces separating them. The terraces have Si dimer rows oriented parallel to the step edge [33]. LEED shows a clean (2×1) pattern with only very weak (1×2) spots and characteristic spot splitting due to D_B steps as shown in Fig. A.8 [71], confirming a mostly single

domain. As seen in Fig. A.7, for a couple of hours the sample is unaffected by contamination, with flashing repeated once it has deteriorated.

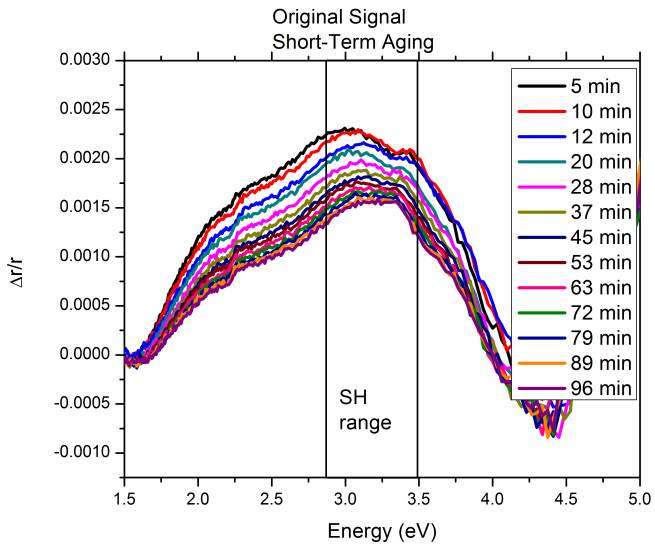

Figure A.7: RAS data showing short time degradation of surface following flashing.

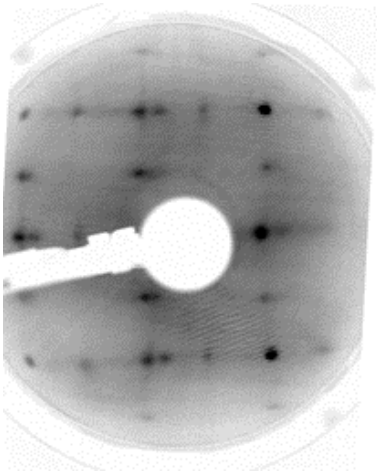

Figure A.8: LEED pattern from a vicinal, reconstructed Si(001)surface using 60 eV electrons. A clear (2×1) reconstruction is visible with only weak (1×2) spots. The characteristic splitting of primary spots is caused by the periodicity of D_B.

We can introduce hydrogen through a precision leak valve on the injection arm and by connecting to a high purity H_2 gas cylinder. The hydrogen is further purified

using a cold trap seen in Fig. A.9 that freezes out any remaining contaminants. We follow the same procedure for deuterium.

Figure A.9: The liquid nitrogen cold trap used to purify gases.

Appendix B: Optical Setup

B.1 Second Harmonic Generation

The fundamental laser beam was produced by an unamplified Ti:Sapphire oscillator which produces laser pulses of around 120 fs FWHM at a repetition rate of 76 MHz with a spectral range of 740 840 nm. The original power intensity of 1.2 W was reduced to about 200 mW before focused on the sample through laser beam suitable windows at a number of incidence angles as shown in Fig. B.1. The spot size radius of the sample is about $30\mu m$. Two Hamamatsu PMTs were used to measure the resulting SHG and a reference SHG. More information is shown in Tab. B.1. To achieve polarization rotation, a Teensy USB Arduino device was used to control an Oriel stepper controller which, in turn, controls the rotation of a polarizer or a half-wave plate.

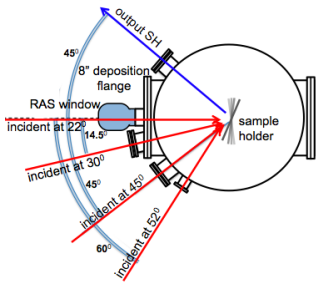

Figure B.1: The optical ports for SHG at 22°,30°,45°,and 52° degrees.

Name	Manufacturer	Description
PMT	Hamamatsu	R4220P
pre-amplifier	Stanford Research	
Ti:Sapphire laser	Coherent	MIRA, 76MHz, 150fs, 700-880nm, 1.5W
Photon counter	Stanford Research	SR-400
motorized mirrors	NewFocus	PicoMotor 8807, iPico Driver 8753
USB webcam	Logitech	
stepper motor	VG Scienta	
stepper motor controller	Intelligent Systems	Panther LI
Rotation motor controller	Oriel	controls rotation of incoming and observing polarization
Teensy 2.0	PJRC	USB Arduino microcontroller

Table B.1: Components of the second harmonic setup

B.2 Rotational Anisotropy Spectroscopy

Reflectance Anisotropy Spectroscopy was developed by Aspnes et al. in 1985 [36] and it works by measuring the difference in reflectance (r) of normal incidence plane-polarized light between two orthogonal directions in the surface plane (-110,110) normalized to the mean reflectance (r). Thus, when the bulk is isotropic and the surface anisotropic we can observe the anisotropy of the surface. The two reflected polarizations pass though a piezoelastic modulator that impedes a phase difference which is then turned into intensity difference by the analyzer. The real part is measured by the LIA at 100KHz and the imaginary by the LIA at 50 KHz.

The RAS setup was originally built by L.M. Mantese. A top-down view is shown in Fig. B.3 where the major components can be seen. The light is produced by a Xenon lamp with a spectral range of 1.5 - 5.5 eV which is then focused by a

30cm focal length mirror through a Rochon polarizer. The light, which is linearly at an angle of 45 degrees with respect to [110] of the sample, is reflected through a photoelastic modulator oscillating at 50 KHz and an analyzer. It is then spectrally resolved by a spectrometer and detected by a photon multiplier tube. The detected signal consists of a very small modulated part (AC) and a large DC part. The modulated part is extracted by using a lock-in amplifier and is proportional to the difference in reflectance between the two axes. The signal is then sent to the computer for recording.

The system was re-built by the author and undergraduate research assistant Jesse Stamper. The main improvements were an complete re-write of the controlling program, the replacement of the PMT with a more efficient and much smaller one and the use of a modern data acquisition system compatible with the Labview program. Also the DC-feedback loop was re-built and an external sample strain setup was built. In Fig. B.2 the RAS electronics setup is presented. Major components are presented in Table B.2.

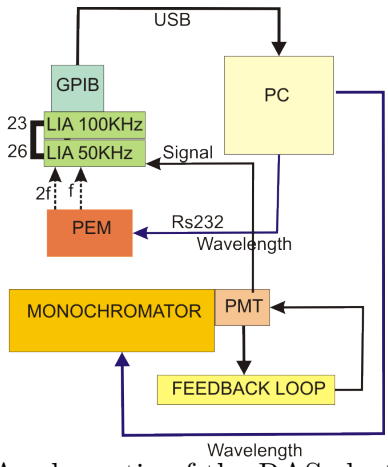

Figure B.2: A schematic of the RAS electronics setup.


Figure B.3: A top-down view of the RAS setup.

Name	Manufacturer	Description
PEM	Hinds Instruments	PEM-90, serial number 0971-0, f250 KHz
lamp housing	Oriel/Newport	part number 60005
Xenon lamp	Hamamatsu	XB075W/2
Lock-in amplifier	Stanford Research	SR-510
Monochromator	McPherson	stepper motor controlled grating, model 234/302
stepper motor controller	McPherson	model 789A
feedback loop	home-built	
pre-amplifier	home-built	
HV power supply	McPherson	model 7640, operated in feedback loop to keep DC signal at 0.5V over the whole spectral range
DAQ	National Instruments	NI-DAQ 150
PMT	Hamamatsu	R374, head/R928, side-on

Table B.2: Components of the rotational anisotropy spectroscopy setup

Bibliography

[1] R. Ehlert. *Epioptics of stepped silicon surfaces*. PhD thesis, The University of Texas at Austin, 2011.

[2] J. Kwon. *Second-harmonic generation and reflectance-anisotropy spectroscopy of vicinal Si(001)*. PhD thesis, The University of Texas at Austin, 2006.

[3] Lalani K. et al. Observation of second-harmonic generation induced by pure spin currents. *Nature Physics*, 6(11):875–878, 2010.

[4] M. Lawrenz and et al. Diffusion pathways of hydrogen across the steps of a vicinal si(001) surface. *Physical Review B*, 75(12), 2007.

[5] Prem A. Study of applications of second harmonic generation. Master's thesis, The University of Texas at Austin, 2011.

[6] G. P. Lopinski, R. A. Wolkow, and D. D. M. Wayner. Self-directed growth of molecular nanostructures on silicon. *Nature*, 406(6791):48–51, 2000.

[7] D. E. Barlow, S. C. Erwin, A. R. Laracuente, J. N. Russell, and L. J. Whitman. Site-specific chemistry of ethylene on si(114)-(2 1). *Journal of Physical Chemistry C*, 112(9):3349–3357, 2008.

[8] P. A. Franken, A. E. Hill, C. W. Peters, and G. Weinreich. Generation of optical harmonics. *Physical Review Letters*, 7(4):118–119, 1961.

[9] Nicolaas Bloembergen, J. A. Armstrong, J. Ducuing, and P. S. Pershan. Interactions between light waves in a nonlinear dielectric. *The physical review : a journal of experimental and theoretical physics*, 127(6):1918–1939, 1962.

[10] Nicolaas Bloembergen and P. S. Pershan. Light waves at the boundary of nonlinear media. *The physical review : a journal of experimental and theoretical physics*, 128(2):606–622, 1962.

[11] R. W. Terhune, P. D. Maker, and C. M. Savage. Optical harmonic generation in calcite. *Physical Review Letters*, 8(10):404–406, 1962.

[12] J. Ducuing and N. Bloembergen. Observation of reflected light harmonics at the boundary of piezoelectric crystals. *Physical Review Letters*, 10(11):474–476, 1963.

[13] Fielding Brown, Robert E. Parks, and Arthur M. Sleeper. Nonlinear optical reflection from a metallic boundary. *Physical Review Letters*, 14(25):1029–1031, 1965.

[14] Fielding Brown and Robert E. Parks. Magnetic-dipole contribution to optical harmonics in silver. *Physical Review Letters*, 16(12):507–509, 1966.

[15] R. K. Chang, J. Ducuing, and N. Bloembergen. Relative phase measurement between fundamental and second-harmonic light. *Physical Review Letters*, 15 (1):6–8, 1965.

[16] Sudhanshu S. Jha. Theory of optical harmonic generation at a metal surface. *Physical Review*, 140(6A):A2020–A2030, 1965.

[17] N. Bloembergen, R. K. Chang, and C. H. Lee. Second-harmonic generation of light in reflection from media with inversion symmetry. *Physical Review Letters*, 16(22):986–989, 1966.

[18] N. Bloembergen, R. K. Chang, S. S. Jha, and C. H. Lee. Optical second-harmonic generation in reflection from media with inversion symmetry. *Physical Review*, 174(3):813–822, 1968.

[19] J. F. McGilp. A review of optical second-harmonic and sum-frequency generation at surfaces and interfaces. *Journal of Physics D: Applied Physics*, 29:1812, 1996.

[20] G. L. Richmond, J. M. Robinson, and V. L. Shannon. Second harmonic generation studies of interfacial structure and dynamics. *Progress In Surface Science*, 28:1–70, 1988. doi: 10.1016/0079-6816(88)90005-6.

[21] W. K. Burton, N. Cabrera, and F. C. Frank. The growth of crystals and the equilibrium structure of their surfaces. *Philosophical Transactions of the Royal Society of London. Series A, Mathematical and Physical Sciences*, 243(866):299–358, 1951.

[22] Hyeong-Chai Jeong and Ellen D. Williams. Steps on surfaces: experiment and theory. *Surface Science Reports*, 34(6):171–294, 1999.

[23] K. Mizuguchi, N. Hayafuji, S. Ochi, T. Murotani, and K. Fujikawa. Mocvd gaas growth on ge (100) and si (100) substrates. *Journal of Crystal Growth*, 77: 509–514, September 1986. doi: 10.1016/0022-0248(86)90345-3.

[24] A. J. Hoeven, J. M. Lenssinck, D. Dijkkamp, E. J. van Loenen, and J. Dieleman. Scanning-tunneling-microscopy study of single-domain si(001) surfaces grown by molecular-beam epitaxy. *Physical Review Letters*, 63(17):1830–1832, 1989.

[25] M. Henzler and J. Clabes. In *Proc. 2nd Int. Conf. Solid Surfaces*, volume 2 of *Jpn. J. Appl. Phys. Suppl.*, page 398, 1974.

[26] Christoph Tegenkamp. Vicinal surfaces for functional nanostructures. *Journal of Physics: Condensed Matter*, 21(1):013002, 2009.

[27] F. J. Himpsel, A. Kirakosian, J. N. Crain, J. . Lin, and D. Y. Petrovykh. Self-assembly of one-dimensional nanostructures at silicon surfaces. *Solid State Communications*, 117(3):149–157, 2001.

[28] Y. R. Shen. Surface properties probed by second-harmonic and sum-frequency generation. *Nature*, 337(6207):519–525, 1989.

[29] G. D. Powell, J.-F. Wang, and D. E. Aspnes. Simplified bond-hyperpolarizability model of second harmonic generation. *Phys. Rev. B*, 65:205320, May 2002. doi: 10.1103/PhysRevB.65.205320. URL `https://link.aps.org/doi/10.1103/PhysRevB.65.205320`.

[30] Z. Sobiesierski, D. I. Westwood, and C. C. Matthai. Aspects of reflectance anisotropy spectroscopy from semiconductor surfaces. *Journal of Physics: Condensed Matter*, 10:1, 1998.

[31] D. E. Aspnes. Bond models in linear and nonlinear optics. *physica status solidi (b)*, 247(8):1873–1880, 2010.

[32] G. Lpke, D. J. Bottomley, and H. M. van Driel. Second- and third-harmonic generation from cubic centrosymmetric crystals with vicinal faces: phenomenological theory and experiment. *Journal of the Optical Society of America B*, 11 (1):33–44, 1994.

[33] Z. J. Donhauser, B. A. Mantooth, K. F. Kelly, L. A. Bumm, J. D. Monnell, J. J. Stapleton, D. W. Price, A. M. Rawlett, D. L. Allara, J. M. Tour, and P. S. Weiss. Conductance switching in single molecules through conformational changes. *Science*, 292(5525):2303–2307, 2001.

[34] Giovanni Costantini, Klaus Kern, and Johannes V. Barth. Engineering atomic and molecular nanostructures at surfaces. *Nature*, 437(7059):671–679, 2005.

[35] G. Kresse and J. Hafner. Ab initio molecular-dynamics simulation of the liquid-metalamorphous-semiconductor transition in germanium. *Physical Review B*, 49 (20):14251–14269, 1994.

[36] D. E. Aspnes and A. A. Studna. Anisotropies in the aboveband-gap optical spectra of cubic semiconductors. *Physical Review Letters*, 54(17):1956–1959, 1985.

[37] G. M. Gavaza, Z. X. Yu, L. Tsang, C. H. Chan, S. Y. Tong, and M. A. Van Hove. Efficient calculation of electron diffraction for the structural determination of nanomaterials. *Phys. Rev. Lett.*, 97:055505, Aug 2006. doi: 10.1103/PhysRevLett.97.055505.

[38] G. M. Gavaza, Z. X. Yu, L. Tsang, C. H. Chan, S. Y. Tong, and M. A. Van Hove. unpublished.

[39] C. J. Davisson and L. H. Germer. *Phys. Rev. 30*, 705, 1927.

[40] Z.G. Pinsker. Electron diffraction. *Butterworths Scientific Publications*, page 394, 1953.

[41] J.J. Lander et al. Low energy electron diffraction study of silicon surface structures. *J. Chem. Phys.*, 37:729, 1962.

[42] H.E. Farnsworth et al. tructure and adsorption characteristics of clean surfaces of germanium and silicon. *J. Chem. Phys.*, 30:917, 1959.

[43] Wayne T. Sproull. A new type of apparatus for experiments in secondary electron diffraction. *Review of Scientific Instruments*, 4(4):193–196, 1933. doi: 10.1063/1.1749100.

[44] J. J. Lander, J. Morrison, and F. Unterwald. Improved design and method of operation of low energy electron diffraction equipment. *Review of Scientific Instruments*, 33(7):782–783, 1962. doi: 10.1063/1.1717975.

[45] W. Ehrenberg. A new method of investigating the diffraction of slow electrons by crystals. *Philos. Mag.*, 18:878, 1934.

[46] Jr. C. W. Caldwell. Double grid repeller system to improve electron resolution in low energy electron diffraction equipment. *Review of Scientific Instruments*, 36(10):1500–1501, 1965. doi: 10.1063/1.1719369.

[47] Robert L. Park and H. E. Farnsworth. Pulsed-beam low energy electron diffraction system for rapid precision measurements. *Review of Scientific Instruments*, 35(11):1592–1596, 1964. doi: 10.1063/1.1719217.

[48] L. H. Germer. Low energy electron diffraction. *Phys. Today*, 17(7):19, 1964.

[49] Takuji Komura, Takafumi Yao, and Masamichi Yoshimura. Atomic and electronic structures of rebonde db-type steps on the si(001)21 surface. *Physical Review B*, 56(7):3579–3582, 1997.

[50] E. Pehlke and P. Kratzer. Density-functional study of hydrogen chemisorption on vicinal si(001) surfaces. 1998.

[51] W. Lu, W.G. Schmidt, and J. Bernholc. Cycloaddition reaction versus dimer cleavage at the Si(001):C_5H_8 interface. *Physical Review B*, 68(11):115327, September 2003. doi: 10.1103/PhysRevB.68.115327.

[52] Stacey F. Bent. Organic functionalization of group iv semiconductor surfaces: principles, examples, applications, and prospects. *Surface Science*, 500(1):879–903, 2002.

[53] F. J. Himpsel, J. L. McChesney, J. N. Crain, A. Kirakosian, V. Prez-Dieste, Nicholas L. Abbott, Yan-Yeung Luk, Paul F. Nealey, and Dmitri Y. Petrovykh. Stepped silicon surfaces as templates for one-dimensional nanostructures. *The Journal of Physical Chemistry B*, 108(38):14484–14490, 2004.

[54] D. J. Chadi. Stabilities of single-layer and bilayer steps on Si(001) surfaces. *Physical Review Letters*, 59(15):1691–1694, 1987.

[55] Victor Mizrahi and J. E. Sipe. Phenomenological treatment of surface second-harmonic generation. *Journal of the Optical Society of America B*, 5(3):660–667, 1988.

[56] R. A. Wolkow. Controlled molecular adsorption on silicon: laying a foundation for molecular devices. *Annual review of physical chemistry*, 50(1):413–441, 1999.

[57] Sukmin Jeong and Atsushi Oshiyama. Structural stability and adatom diffusion at steps on hydrogenated Si(100) surfaces. *Physical Review Letters*, 81(24):5366–5369, 1998.

[58] Bilal Gokce, Eric J. Adles, David E. Aspnes, and Kenan Gundogdu. Measurement and control of in-plane surface chemistry during the oxidation of h-terminated (111) si. *Proceedings of the National Academy of Sciences of the United States of America*, 107(41):17503–17508, 2010.

[59] Jinhee Kwon and M. C. Downer. Reflectance-difference and second-harmonic generation: a meeting of two surface spectroscopies. *Physica Status Solidi*, (8): 3055–3059, 2003.

[60] Robert J. Hamers. Formation and characterization of organic monolayers on semiconductor surfaces. *Annual review of analytical chemistry (Palo Alto, Calif.)*, 1(1):707–736, 2008.

[61] Shinichi Machida, Kanae Hamaguchi, Masashi Nagao, Fumiko Yasui, Kozo Mukai, Yoshiyuki Yamashita, Jun Yoshinobu, Hiroyuki S. Kato, Hiroshi Okuyama, and Maki Kawai. Electronic and vibrational states of cyclopentene on Si(100)(21). *The Journal of Physical Chemistry B*, 106(7):1691–1696, 2002.

[62] C. Ohlhoff, G. Lpke, C. Meyer, and H. Kurz. Static and high-frequency electric fields in silicon mos and ms structures probed by optical second-harmonic generation. *Physical Review B*, 55(7):4596–4606, 1997.

[63] Nathan P. Guisinger, Nathan L. Yoder, Mark C. Hersam, and Mark A. Ratner. Probing charge transport at the single-molecule level on silicon by using cryogenic ultra-high vacuum scanning tunneling microscopy. *Proceedings of the National Academy of Sciences of the United States of America*, 102(25):8838–8843, 2005.

[64] Wolfgang Richter and J. F. McGilp. Optical in situ surface control during movpe and mbe growth [and discussion]. *Philosophical Transactions: Physical Sciences and Engineering*, 344(1673):453–467, 1993.

[65] R. J. Hamers, S. K. Coulter, M. D. Ellison, J. S. Hovis, D. F. Padowitz, M. P. Schwartz, C. M. Greenlief, and J N Russell, Jr. Cycloaddition chemistry of organic molecules with semiconductor surfaces. *Accounts of chemical research*, 33(9):617–624, 2000.

[66] Jinhee Kwon. *Second-harmonic generation and reflecance-anisotropy spectroscopy of vicinal Si(001)*. PhD thesis, 2006.

[67] A. R. Laracuente and L. J. Whitman. Step structure and surface morphology of hydrogen-terminated silicon: (001) to (114). *Surface Science*, 545(1):70–84, 2003.

[68] Hendradi Hardhienata. Modeling fourth harmonic generation in a non-vicinal (111) diamond lattice. *IOP Conference Series: Materials Science and Engineering*, 166(1):012012, 2017.

[69] R.W. Kempf, P.T. Wilson, J.D. Canterbury, E.D. Mishina, O.A. Aktsipetrov, and M.C. Downer. Third and fourth harmonic generation at si-sio2 interfaces and in si-sio2-cr mos structures. *Applied Physics B*, 68(3):325–332, Mar 1999. ISSN 1432-0649. doi: 10.1007/s003400050627.

[70] F Jona et al. *Rep. Prog. Phys.*, 45:527, 1982.

[71] Jinhee Kwon, M. C. Downer, and B. S. Mendoza. Second-harmonic and reflectance-anisotropy spectroscopy of vicinal Si(001)-Sio2 interfaces: Experiment and simplified microscopic model. *Physical Review B*, 73(19), 2006.

Vita

Loucas Loumakos was born in Nicosia, Cyprus by Kipros and Maria Loumakou. After completing Lyceum he served in the Cyprus National Guard as a Sergeant for two years before attending the Physics Department of the University of Cyprus. In May 2004 he received his Bachelor of Science in Physics and in May 2006 the Magister Scientae in Physics working with the group of Prof. Andreas Othonos. He entered the Ph.D. program of the Physics Department of The University of Texas at Austin in August 2008 where he later joined the Epioptics group of Prof. Michael Downer. During his graduate studies in Austin he met and married Lauren Eleftheriou.

Email Address: **loucas@loumakos.com**

This dissertation was typeset with LaTeX [1] by the author.

[1] LaTeXis a document preparation system developed by Leslie Lamport based on Dondals Knuth's TeX.